Global impact of nitrate photolysis in sea-salt aerosol on NO$_x$, OH, and O$_3$ in the marine boundary layer

Prasad Kasibhatla[1], Tomás Sherwen[2,3], Mathew J. Evans[2,3], Lucy J. Carpenter[2], Chris Reed[2,4], Becky Alexander[5], Qianjie Chen[5], Melissa Sulprizio[6], James D. Lee[2], Katie A. Read[2], William Bloss[7], Leigh R. Crilley[7], William C. Keene[8], Alex A. P. Pszenny[9], Alma Hodzic[10,11]

[1]Nicholas School of the Environment, Duke University, Durham, NC 27708, USA
[2]Wolfson Atmospheric Chemistry Laboratories, Department of Chemistry, University of York, York YO10 5DD, UK
[3]National Centre for Atmospheric Science, University of York, York YO10 5DD, UK
[4]Facility for Airborne Atmospheric Measurements (FAAM), Cranfield University, Cranfield, MK43 0AL, UK
[5]Department of Atmospheric Sciences, University of Washington, Seattle, WA 98195, USA
[6]School of Engineering and Applied Sciences, Harvard University, Cambridge, MA 02138, USA
[7]School of Geography, Earth and Environmental Sciences, University of Birmingham, Edgbaston, Birmingham, B15 2TT, UK
[8]Department of Environmental Sciences, University of Virginia, Charlottesville, VA, 22904, USA
[9]Institute for the Study of Earth, Oceans, and Space, University of New Hampshire, Durham, NH 03824, USA
[10]National Center for Atmospheric Research, Boulder, CO 80305, USA
[11]Laboratoire d'Aérologie, Université de Toulouse, CNRS, University Paul Sabatier, France

Correspondence to: Prasad Kasibhatla (psk9@duke.edu)

Abstract. Recent field studies have suggested that sea-salt particulate nitrate (NITs) photolysis may act as a significant local source of nitrogen oxides (NO$_x$) over oceans. We present a study of the global impact of this process on oxidant concentrations in the marine boundary layer using the GEOS-Chem model, after first updating the model to better simulate observed gas/particle phase partitioning of nitrate in the marine boundary layer. Model comparisons with long-term measurements of NO$_x$ from the Cape Verde Atmospheric Observatory (CVAO) in the eastern tropical North Atlantic provide support for an *in situ* source of NO$_x$ from NITs photolysis, with NITs photolysis coefficients about 25-50 times larger than corresponding HNO$_3$ photolysis coefficients. Short-term measurement of nitrous acid (HONO) at this location show a clear daytime peak, with average peak mixing ratios ranging from 3 to 6 pptv. The model reproduces the general shape of the diurnal HONO profile only when NITs photolysis is included, but the magnitude of the daytime peak mixing ratio is under-predicted. This under-prediction is somewhat reduced if HONO yields from NITs photolysis are assumed to be close to unity. The combined NO$_x$ and HONO analysis suggests that the upper limit of the ratio of NITs:HNO$_3$ photolysis coefficients is about 100. The largest simulated relative impact of NITs photolysis is in the tropical and subtropical marine boundary layer, with peak local enhancements ranging from factors of 5-20 for NO$_x$, 1.2-1.6 for OH, and 1.1-1.3 for ozone. Since the spatial extent of the sea-salt aerosol impact is limited, global impacts on NO$_x$, ozone and OH mass burdens are small (~1-3 %). We also present preliminary analysis showing that particulate nitrate photolysis in accumulation-mode aerosols (predominantly over continental regions) could lead to ppbv-level increases in ozone in the continental boundary layer. Our results highlight the

need for more comprehensive long-term measurements of NO_x, and related species like HONO and sea-salt particulate nitrate, to better constrain the impact of particulate nitrate photolysis on marine boundary layer oxidant chemistry. Further field and laboratory studies on particulate nitrate photolysis in other aerosol types are also needed to better understand the impact of this process on continental boundary layer oxidant chemistry.

5 **1 Introduction**

Nitrogen oxides (NO_x) are a key component of tropospheric chemistry due to their impact on oxidant chemical cycles. This paper focuses on the NO_x budget of the marine boundary layer (MBL). The traditional view has been that relatively low concentrations of NO_x in the MBL are maintained by a balance between the transport of NO_x to the MBL (either by direct transport of NO_x from continental source regions or by transport and subsequent decomposition of NO_x reservoirs such as
10 organic nitrates) and chemical destruction by reaction with hydroxyl radicals (OH) (e.g., Moxim et al., 1996). NO_x emissions from ships (Lawrence and Crutzen, 1999; Kasibhatla et al., 2000; Beirle et al., 2004), downward transport of lightning-produced NO_x from the free troposphere (Levy et al., 1996, 1999), and halogen-mediated chemistry (von Glassow et al., 2004; Keene et al., 2009; Long et al., 2014; Schmidt et al., 2016; Sherwen et al., 2016a, 2016b) also modulate NO_x levels in the MBL.

Past laboratory studies have suggested that recycling of NO_x by photochemical reactions of adsorbed nitrate on surfaces might also serve as an *in situ* NO_x source (e.g. Zhou et al., 2003; Handley et al. 2007; Chen et al., 2011; Laufs and Kleffmann, 2016). More recently, field studies have suggested that photolysis of particulate nitrate (p-NO_3) associated with MBL sea-salt aerosols (SSA) can be a significant source of NO_x. In particular, Ye et al. (2016) analyzed trace gas measurements from two aircraft
20 flights over the western subtropical North Atlantic Ocean during the summer 2013 Nitrogen, Oxidants, Mercury and Aerosol Distributions, Sources and Sinks (NOMADSS) field campaign and hypothesized that measured daytime nitrous acid (HONO) concentrations in the MBL were indicative of a significant *in situ* source from p-NO_3 photolysis (since HONO photolyses rapidly to yield NO_x, p-NO_3 photolysis is effectively a NO_x source). Their box model analysis suggested that the peak p-NO_3 photolysis rate coefficient was of the order of 2×10^{-4} s^{-1}, about 300 times larger than the corresponding photolysis coefficient
25 for gas-phase nitric acid (HNO_3). Manipulation experiments involving irradiation of samples of ambient (Ye et al., 2016, 2017b) and synthetic marine aerosol (Zhou et al., 2008) provide additional support for the hypothesized importance of p-NO_3 photolysis in the MBL. It is also worth noting that photolysis of nitrate in seawater has been measured at naturally occurring concentrations, albeit at much lower rates with photolysis rate coefficients averaging 2×10^{-8} s^{-1} (Zafiriou and True, 1979).

30 Measurements of NO_x and HONO at the Cape Verde Observatory in the tropical eastern Atlantic Ocean (CVAO, 16.864^o N, 24.868^o W) have provided additional evidence for *in situ* NO_x production in the MBL (Reed et al., 2017). Long-term NO_x measurements at CVAO show a consistent diurnal cycle, with peak daytime mixing ratios 10-15 pptv higher than night-time

levels in all seasons except in winter (Reed et al., 2017). Shorter term HONO measurements from CVAO also show a strong diurnal cycle, peaking at a few pptv around midday and dropping to near zero at night (Reed et al., 2017). The observed levels of HONO again indicate an *in situ* source, while the diurnal cycle suggests that this source is photolytic. Box model analysis of the CVAO measurements indeed indicate that rapid recycling of NO_x via p-NO_3 photolysis is an important source of NO_x

5   in the tropical MBL, though estimated p-NO_3 photolysis rate coefficients were only 10-15 times larger than HNO_3 photolysis rate coefficients. (Reed et al., 2017; Ye et al., 2017). While some of the variability in estimated p-NO_3 photolysis rates between the NOMADSS and CVAO analyses may be due to differences in SSA composition at the two locations (Ye et al., 2017), the limited measurements preclude from definitive conclusions in this regard.

10   In this paper, we explore the global-scale significance of this newly-recognized p-NO_3 photolysis mechanism for tropospheric oxidant chemistry using the GEOS-Chem global chemical transport model. We perform a series of simulations to assess the sensitivity of NO_x to the rate of p-NO_3 photolysis in SSA in the MBL, and attempt to constrain the magnitude of this *in situ* NO_x source using NO_x and HONO measurements from CVAO. We then estimate the impact of p-NO_3 photolysis on the large-scale distribution of NO_x, O_3 and OH in the MBL. Finally, we perform an initial analysis of the impact of photolysis of nitrate

15   on other aerosol types and consider its implications for continental boundary layer oxidant chemistry.

2 Models and measurements

2.1 GEOS-Chem model configuration

We use the GEOS-Chem chemical transport model (v10-01, Bey et al., 2001; www.geos-chem.org), as updated by Sherwen et al. (2017). The model includes a comprehensive tropospheric NO_x-VOC-HO_x-O_x oxidant chemistry scheme (Mao et al.,

20   2013), coupled to an aerosol module that includes inorganic sulfate, ammonium, and nitrate aerosols (Park et al., 2004), as well as primary black carbon, organic carbon, dust, and sea-salt aerosols (Park et al, 2003; Fairlie et al., 2007; Alexander et al., 2005). The oxidant chemistry scheme also includes a detailed treatment of tropospheric halogen chemistry (Parrella et al., 2012; Schmidt et al., 2016; Sherwen et al. 2016a, 2016b, 2017). Trace gas and aerosol emissions are specified as described in Ford and Heald (2012).

The model transports two size classes of SSA, representing accumulation-mode (0.01-0.5 μm dry radius) and coarse-mode (0.5-8 μm dry radius) SSA. Emissions of SSA are calculated online in the model using the formulation of Gong et al. (2003), as described by Jaeglé et al. (2011). The model explicitly tracks particulate sulfate and nitrate associated with coarse-mode SSA (identified as "SO_4s" and "NITs", respectively, in the model), with SO_4s production and gas-phase HNO_3 uptake (to form

30   NITs) calculated as described by Alexander et al. (2005). In this scheme, SO_4s and NITs formation at each time step is determined by the mass flux of gas-phase sulfur dioxide and HNO_3 to coarse-mode SSA, but limited by the local alkalinity

emission flux in that time step. In Section 3.1, we show that this imposed alkalinity limitation unrealistically limits NITs production in the MBL. We therefore update the model calculation of HNO₃ uptake on coarse-mode SSA as described below.

Laboratory measurements (e.g. Guimbaud et al., 2002) and field studies (e.g. Keene et al., 2009) indicate that freshly produced SSA are rapidly acidified via incorporation of HNO₃ and other acids leading to the volatilization of hydrochloric acid in accordance with expectations based on respective thermodynamic properties (Henry's Law and dissociation constants) and associated meteorological conditions (relative humidity and temperature). We therefore updated the model to calculate HNO₃ uptake (and concomitant NITs production) by coarse-mode SSA using the mass transfer equation appropriate for the transition regime as in Feng and Penner (2007):

$$-\frac{d}{dt}[HNO_3] = \frac{d}{dt}[NITs] = 4\,\pi\,D_g\,R_{cSSA}\,N_{cSSA}\,f(Kn)\,([HNO_3] - [HNO_3]^{eq}) \tag{1}$$

where, [.] represents mixing ratio, D_g is the gas-phase diffusivity of HNO₃, R_{cSSA} is the radius of coarse-mode SSA, N_{cSSA} is the number concentration of coarse-mode SSA, and Kn is the Knudsen number. $[HNO_3]^{eq}$ is the equilibrium concentration of gas-phase HNO₃ associated with coarse-mode SSA, determined using ISORROPIA II (Fountoukis and Nenes, 2007). Since the model does not include aerosol microphysics, R_{cSSA} and N_{cSSA} are estimated from effective dry radius and mass concentration of coarse-mode SSA, assuming a dry SSA density of 2200 kg m⁻³ and using relative humidity dependent SSA growth factors (Lewis and Schwartz, 2006). The function $f(Kn)$ is the ratio of gas-phase flux to the particle in the transition region to that in the continuum regime, and is specified using the Fuchs and Sutugin (1971) formulation:

$$f(Kn) = \frac{0.75\,\alpha\,(1 + Kn)}{Kn^2 + Kn + 0.283\,Kn\,\alpha + 0.75\,\alpha} \tag{2}$$

where, α is the HNO₃ mass accommodation coefficient, specified to be 0.2 (Jacob, 2000).

We evaluate the effect of p-NO₃ photolysis in SSA in the MBL by including the photolysis of NITs (yielding HONO and NO₂) in our updated model. We note that NITs only corresponds to p-NO₃ associated with coarse-mode SSA. The current version of the GEOS-Chem model also tracks p-NO₃ associated with accumulation-mode aerosols (identified as "NIT" in the model), but does not track the fraction that is specific to accumulation-mode SSA. We therefore do not include photolysis of accumulation-mode p-NO₃ in our analysis of MBL SSA nitrate photolysis. We discuss the implication of this model limitation in Section 3.1. We also present results of a sensitivity simulation designed to explore the effect of accumulation-mode NIT photolysis on continental boundary layer composition in Section 3.4.

Following the empirical analysis of Ye et al. (2016), the NITs photolysis rate coefficient (J_{NITs}) is scaled to the photolysis rate of HNO₃ (J_{HNO_3}). We refer to this scaling coefficient as J_{scale} in the rest of this paper. Box model analyses of measurements from NOMADSS, the spring 2007 Reactive Halogens in the Marine Boundary Layer (RHaMBLe) project, and measurements made at Cape Verde suggest J_{scale} values of between 10-300 (Ye et al., 2016; Reed et al., 2017; Ye et al., 2017), with the variability possibly related to differences in SSA composition at different locations in the MBL (Ye et al., 2017). In light of

this uncertainty, we show model results for a range of J_{scale} values, and use measurements of NO_x and HONO from CVAO to estimate reasonable bounds for this scaling factor. In the subsequent discussion, we use the notation J_{scale}^n, where the superscript n indicates the value of J_{scale}. Note that in this notation, J_{scale}^0 refers to the 'no NITs photolysis' case. NITs photolysis is initially assumed to yield HONO and NO_2 in the molar ratio of 0.67:0.33 (Ye et al., 2016; Reed et al., 2017), but
5 we also present results from a subset of sensitivity simulations with the HONO:NO_2 molar yield set to 0.93:0.07 (Ye et al., 2017).

The current version of the model does not include a dry deposition term for HONO. While neglecting this term might have a small effect on simulated night-time HONO concentrations in the MBL, the impact should be negligible in terms of simulated
10 daytime HONO concentrations because the lifetime of HONO during the day is controlled by photolysis and not by dry deposition. Dry deposition velocities for species with Henry's law coefficients similar to HONO are typically 0.5-1 cm s^{-1} over oceans. For a daytime MBL depth of 1 km, this corresponds to a lifetime against dry deposition of about 1-2 days. By contrast, HONO has a lifetime of minutes against photolysis during the day at a location like CVAO.

2.2 Measurements used for model evaluation

15 **2.2.1 MBL NITs and HNO$_3$ measurements in the eastern Atlantic Ocean**

During the RHaMBLe field campaign in May and June 2007, volatile water-soluble nitrate (dominated by and hereafter referred to as HNO$_3$) was sampled from the top of the CVAO tower over 2-hour intervals at nominal flow rates of 20 L min^{-1} using tandem mist chambers (MCs), each of which contained 20 ml deionized water (Keene et al., 2009). To minimize artifact phase changes caused by mixing chemically distinct aerosol size fractions on bulk prefilters, air was sampled through a size-
20 fractionating inlet that inertially removed super-µm-diameter aerosols from the sample stream. Sub-µm aerosol was removed downstream by an in-line 47-mm Teflon filter (Zefluor 2-µm pore diameter) that was changed daily. Samples were analyzed on site by ion chromatography (IC) usually within a few hours after recovery. Data were corrected based on dynamic handling blanks that were loaded, briefly (few seconds) exposed to ambient air flow, recovered, processed, and analyzed using procedures identical to those for samples. Collection efficiencies were greater than 95 % and, consequently, corrections for
25 inefficient sampling were not necessary. Relative precisions based on paired measurements varied as functions of concentration and typically averaged ±10 % to ±25 %. The average detection limit (DL; estimated following Keene et al. (1989)) was 12 pptv. Longer-term aerosol nitrate measurements were also made at CVAO, as part of a larger suite of aerosol measurements. Samples were collected on quartz-fibre filters using high-volume sampler with a PM10 inlet, and were subsequently analysed by ion-chromotography. Here, we use the measurement summaries for summer marine air masses from 2007-2011 reported
30 by Fomba et al. (2014).

During October and November 2003, the German research ship *Polarstern* cruised along a latitudinal transect through the eastern Atlantic Ocean from Germany to South Africa. HNO_3 was measured from the ship at approximately 23 m above the water line over 2-hour intervals using the same MC-IC technique described above. The average DL was 2 pptv. During this cruise, ambient aerosols were also sampled in parallel over discrete daytime and nighttime intervals using a modified Graseby-Anderson Model 235 cascade impactor configured with a Liu-Pui type inlet, precleaned polycarbonate substrates, and quartz-fiber backup filters (Pallflex 2500 QAT-UP) (Keene et al., 2009). At an average sampling rate of 0.78 m^3 min^{-1}, the average 50 % aerodynamic cut diameters for the impaction stages were 20, 11, 4.3, 2.5, 1.2, and 0.65 µm. Bulk aerosol was sampled in parallel on quartz-fiber filters at an average flow rate of 1.1 m^3 min^{-1}. Impactors and bulk-filter cassettes were cleaned, dried, loaded, and unloaded in a Class 100 clean bench configured with impregnated filters on the inlet to remove alkaline- and acidic-reactive trace gases. Exposed substrates and filters were halved, transferred to polypropylene tubes, sealed in glass mason jars, frozen, and express shipped from Cape Town to the Mount Washington Observatory, NH for analysis. Half sections of each substrate were extracted in 13 ml deionized water using a mini vortexer and sonication; half sections of exposed backup and bulk filters were similarly extracted in 40 ml deionized water. Substrate and filter extracts was analyzed by IC for major ionic species including NO_3^- and Na^+. The corresponding average DLs for bulk samples were 0.04 and 2.6 nmol m^{-3}, respectively; those for the GMD 0.46-µm size fraction were 0.05 and 3.5 nmol m^{-3}, respectively; and those for the larger individual size fractions were 0.01 and 0.1 nmol m^{-3}, respectively. Internal losses of super-µm aerosols within slotted cascade impactors of this type average about 25 % to 30 % (e.g. Willeke, 1975); other sources of bias for size-resolved particulate analytes based on the above procedures are generally unimportant (Keene et al., 1990).

2.2.2 Long-term measurements of NO_x and O_3 from CVAO

Ambient air for NO_x and O_3 measurements is drawn from a 40 mm glass manifold (QVF) with a hooded inlet positioned 10 m above ground level at the CVAO site. NO and NO_2 are measured by NO chemiluminescence (Drummond et al., 1985) with NO_2 converted photolytically to NO by illumination at 385-395 nm (Lee et al., 2009). The limits of detection for NO and NO_2 were 0.30 and 0.35 pptv when averaged over an hour, with an accuracy of 5 % and 5.9 % respectively. Reed et al., (2016) showed that in regions that typically have low NO_x concentrations and are cold, *in situ* measurements of NO_2 may be instrumentally biased high due to thermal decomposition of NO_y species such as PAN and HO_2NO_2, leading to apparent perturbations in the Leighton relationship (Leighton 1961). These effects are however considered to be minimal at CVAO (Reed et al., 2016). Ozone (O_3) is measured by a Thermo Scientific model 49i UV photometer which quantifies O_3 by single wavelength absorption at 254 nm along a 38 cm path-length whilst simultaneously determining a zero background measurement in a second absorption cell. The lower detectable limit is 1ppbv.

2.2.3 Short-term measurement of HONO from CVAO and RHaMBle

Measurements of the HONO at CVAO were performed between 24th November and 3rd December 2015 using a LOng Path Absorption Photometer (LOPAP-03 QUMA Elektronik & Analytik GmbH), described in Heland et al. (2001). Briefly, the LOPAP is a wet chemical technique where gas-phase HONO is sampled within a stripping coil into an acidic solution and is derivatized into an azo dye, with the light absorption of the dye at 550 nm measured with a spectrometer. The LOPAP was operated and calibrated according to the standard procedures described in Kleffmann and Wiesen (2008) and was set up at CVAO in order to maximise the sensitivity of the LOPAP, as described in Reed et al. (2017). Regular baseline measurements (8 hrs) using an overflow of high purity N_2 were performed to account for instrument drift. The detection limit (2σ) of the LOPAP was calculated to be 0.2 pptv, with the relative error conservatively set to 10 % of the measured concentration. Kleffmann et al. (2006) have explicitly shown that particle bound nitrite does not give rise to significant interference in the LOPAP. If such a positive bias were to occur, we would expect this to also be apparent at night. The observed low HONO concentration (<1 pptv) at night puts a (low) upper limit on any such contribution.

During RHaMBLe (see Lee et al., 2010; Sander et al., 2013) HONO was measured in parallel with HNO_3 using the same MC-IC technique described above. The average detection limit was 2 pptv. These data are considered semi-quantitative because performance of the MC-IC technique for HONO has not been rigorously evaluated. However, intercomparisons of opportunity with HONO measured in parallel by MC-IC and long-path DOAS during summer 2004 in coastal New England as part of ICARTT (ranging from <45 to 730 pptv; Keene et al., 2006, 2007) and by MC-IC and NI-PT-CIMS during winter 2011 in Colorado as part of NACHTT (ranging from <32 to 200 pptv; VandenBoer et al., 2013) indicate generally good agreement within ±20 %.

2.3 Model simulations

We performed a series of 2-year model simulations (each with a 6-month spin up from a standard GEOS-Chem benchmark simulation) covering the 2014-2015 period, so as to compare with long-term measurements of NO_x and O_3 at CVAO during this period. Given our focus on the MBL, we used the 4° x 5° horizontal resolution version of the model for computational efficiency. The vertical grid is a 47-level hybrid sigma pressure grid, extending from the surface to 80 km. The vertical grid resolution in the lowermost km is about 125-150 m. All simulations used meteorological fields from the Goddard Earth Observation System Forward Processing (GEOS-FP) assimilation system produced by the NASA Global Modeling and Assimilation Office (Luchesi, 2013). Data processing was performed using the open-source python packages Numpy [van der Walt et al., 2011] and Pandas [McKinney, 2010], and figures were prepared using the open-source python plotting packages matplotlib [Hunter et al., 2007] and Seaborn [Waskom et al., 2017]

In the rest of this paper, we refer to the model with the imposed alkalinity limitation to acid uptake as the 'standard' model, and the model with additional nitric acid uptake due to hydrochloric acid displacement (described in Section 2.1) as the 'updated' model.

3. Results and discussion

3.1 Gas-particle partitioning of nitrate in the MBL

Figure 1 shows a comparison of modeled gas-phase HNO_3 and total particulate nitrate (i.e. the sum of NITs and NIT) concentrations with measurements in the tropical eastern North Atlantic for the standard model and for the updated model. We
5   note that the modeled time period does not coincide exactly with the different periods over which the HNO_3 and p-NO_3 measurements were taken, indicated in Fig. 1. However, interannual variability in these regions is typically low (Carpenter et al., 2010), while the changes in HNO_3 and total nitrate concentrations induced by the model update are large. It is clear from Fig. 1 that the standard model does not capture the relative partitioning of nitrate between the gas- and particle- phases in the MBL. In the standard model, most of the nitrate is in the gas-phase, in contrast to the measurements which show that most
10   nitrate is in the particle phase.

The biased simulation of p-NO_3/HNO_3 ratios in the standard model is the result of the imposed alkalinity limitation to acid uptake (see section 2.1). For example, tropical North Atlantic SSA emission fluxes are of the order of 25-50 kg km^{-2} day^{-1} (Jaeglé et al., 2011) and the typical alkalinity of freshly emitted SSA is equal to 0.07 equivalents per kg (Gurciullo et al., 1999).
15   Assuming a 1 km MBL depth, this translates to maximum NITs production rates in the MBL of only 1.7-3.5 pptv hr^{-1} in the standard model. In fact, actual NITs production rates in this scheme will be even lower because of competition with gas-phase sulfur dioxide uptake. These low production rates, coupled with the short lifetime of NITs against deposition, is the cause of the biased simulation of MBL p-NO_3/HNO_3 ratios in the standard model. In the updated model, HNO_3 uptake by coarse-mode SSA continues after alkalinity is titrated due in part to hydrochloric acid displacement (as described in Section 2.1) and the
20   simulation of the MBL nitrate partitioning between gas- and particle phases is much improved. This improvement in the simulation of gas-particle partitioning of nitrate is important in the context of our focus on assessing the large-scale importance of p-NO_3 photolysis on MBL chemistry. While this change improves the model performance, it is evident from Fig. 1 that the model underestimates p-NO_3 concentrations for all of the sites evaluated. Given that the dataset of simultaneous remote oceanic HNO_3 and p-NO_3 observations is small, it is unclear at this stage what could be causing this discrepancy.

We also note that simulated SSA concentrations are in agreement with measurements at CVAO. The Na^+ concentration measurements atop a 30 m tower (40 m above sea level) during RHaMBLE (Lawler et al., 2009) imply a SSA mass concentration of 6-19 μg m^{-3}. Fomba et al. (2014) reported similar SSA concentrations (11 ± 5.5 μg m^{-3}) at the top of the tower over a 5-year period from January 2007 to December 2011. In comparison, the simulated annual-average SSA concentration
30   at the lowest model level (centered ~60 m above sea level) at this location is 12.5 μg m^{-3}.

Figure 2 shows maps of average 2014-2015 simulated surface mixing ratios of HNO_3 and NITs in the MBL for the standard and updated models. Consistent with the discussion above, gas-phase HNO_3 is the dominant form of nitrate in the MBL in the

standard model, with mixing ratios exceeding 100 pptv over ocean basins downwind of major continental NO_x source regions. By contrast, maximum simulated NITs mixing ratios are about 10-20 pptv over ocean basins. The updated acid uptake scheme changes the simulated partitioning of nitrate in the MBL globally. Other than in the immediate vicinity of continental NO_x source regions, simulated nitrate is predominantly associated with the particle phase everywhere in the MBL in the updated model (see also Fig. S1). In the rest of this paper, we use the updated model to assess the effects of NITs photolysis on MBL oxidant chemistry.

As mentioned earlier, the current version of the GEOS-Chem model tracks accumulation-mode p-NO_3, but does not separately track the fraction of this mode that is associated with SSA. Since coarse-mode NITs is the dominant form of modeled p-NO_3 in the MBL in continental outflow regions where concentrations are highest (Figs. 2 and S1), this model limitation is not particularly significant in terms of our analysis of SSA p-NO_3 photolysis. We plan to further evaluate this with a future version of the model that will explicitly track p-NO_3 in accumulation-mode SSA.

3.2 NO_x and HONO diurnal cycles at CVAO

The diurnal variation of NO_x and HONO in the MBL can potentially provide useful information on *in situ* NO_x chemical production and destruction. In the remote MBL, one would expect NO_x concentrations to decrease over the course of the day in the absence of an *in situ* chemical source that peaks during the day, owing to the shorter lifetime against oxidation by OH during daylight hours. Similarly, HONO has a lifetime of the order of minutes against photolysis (e.g. Kraus and Hofzumahaus, 1998), and so a diurnal profile that peaks during the day would provide strong evidence for an *in situ* photochemical source for HONO in the MBL. Measurements at CVAO of NO_x and HONO in air masses representative of relatively aged marine boundary layer air do indeed show HONO and NO_x peaking during the day (Reed et al., 2017). This fact has been used by Reed et al. (2017) and Ye et al. (2017) to argue for an *in situ* source of HONO and NO_x from p-NO_3 photolysis based on box model analysis of measurements. Their analyses are, however, limited by the fact that background NO_x levels cannot be explicitly simulated in a box modeling framework. To overcome this limitation, Reed et al. (2017) modeled the background source of MBL NO_x from PAN decomposition by prescribing a flux of PAN from the free troposphere to the MBL. Ye et al. (2017) constrained background NO_x levels in their analysis by specifying NO_2 mixing ratios after sunrise. Here, we re-analyze the CVAO NO_x and HONO measurements in the context of our three-dimensional model that explicitly simulates transport of NO_x and its precursors.

Figures 3, 4, and 5 show comparisons of simulated diurnal profiles of NO, NO_2, and NO_x with measurements at CVAO. Model results are shown for J_{scale} ranging from 0 (i.e. J_{scale}^0, no NITs photolysis) to 100 (i.e. J_{scale}^{100}). To mimic the fact that air masses arriving at CVAO are representative of aged background MBL air (Read et al., 2008; Carpenter et al., 2010), model results are shown for the grid box to the north-west of CVAO to minimize the effect of fresh NO_x emissions from ship traffic off the coast of north Africa on model-measurement comparisons.

Several aspects of the comparisons shown in these figures are worth noting. In all seasons, except winter, a weak daytime peak is evident in observed NO_x. This peak is the result of a relatively flat NO_2 diurnal cycle, combined with an NO diurnal cycle that peaks strongly during the day. The model has difficulty reproducing the details of this diurnal variation. The shape

5   of the NO diurnal cycle is generally well captured by the model, though peak model NO is generally higher than the measurements when J_{scale} is larger than 25. The modeled NO_2 diurnal cycle consistently shows a daytime minimum in the absence of NITs photolysis, a feature that is not evident in the measurements. Modeled NO_2 agrees better with measurements when J_{scale} is specified to be 25-50, though the exact shape of the NO_2 diurnal cycle is not well simulated. This is, in part, due to the sharp decrease in simulated NO_2 at sunrise, owing to the formation and hydrolysis of halogen nitrates. The absence of

10   this feature in the measurements has been previous noted by Reed et al. (2017). They speculate that this could be because of missing halogen chemistry during night-time and/or during the night/day transition in the model. While there are likely shortcomings in our model's representation of NO/NO_2 chemistry, the diurnal NO_x comparisons (Fig. 5) provide support for an *in situ* source of NO_x from NITs photolysis, with NITs photolysis coefficients about 25-50 times larger than corresponding HNO_3 photolysis coefficients. We compare our estimates of the NITs photolysis coefficient with the corresponding estimates

15   by Reed et al. (2017) and Ye et al. (2017) at the end of this sub-section.

Figure 6 shows comparisons of the modeled HONO diurnal cycle with short-term measurements from the spring 2007 RHamBle campaign and with the November-December 2015 CVAO measurements. The measurements consistently show a strong daytime peak in HONO, with peak median mixing ratios ranging from 3.5 to 5.5 pptv. The model reproduces the

20   observed shape of the HONO profile only when NITs photolysis in included. Further, simulated HONO mixing ratios are less than 0.1 pptv when NITs photolysis is not considered, and the model underestimates peak HONO even for J_{scale}^{100}. It is worth recognizing, however, that simulated HONO mixing ratios at CVAO are roughly proportional to the assumed molar yield (set at 0.67) of HONO from NITs photolysis. This is illustrated by the dashed lines in Fig. 6, showing simulated HONO from J_{scale}^{50} and J_{scale}^{100} sensitivity runs in which the molar yield of HONO from NITs photolysis is increased to 0.93 (with a concomitant

25   reduction of the NO_2 yield to 0.07). The choice of 0.93 for the HONO yield in the sensitivity runs is based on the budget analysis of the RHaMBLe measurements by Ye et al. (2017). Increasing the HONO yield from 0.67 to 0.93 increases peak simulated HONO mixing ratios by about 35 %, bringing them into better agreement with the measurements. We note that changing the relative yields of HONO and NO_x from NITs photolysis does not significantly affect simulated NO_x levels because of the short lifetime of HONO against photolysis to NO.

While our analysis supports the existence of an *in situ* photolytic source of HONO and NO_x in the MBL, we are unable to draw a definitive conclusion on the magnitude of this source. The NO_x comparisons presented here suggests that J_{scale} ranges from 25-50, while the HONO comparisons support a larger value of J_{scale} and/or HONO yields from NITs photolysis being close to unity. In the context of assessing the large-scale impact of NITs photolysis, we therefore conclude that a range of 25-100 is

the most appropriate range for the parameter J_{scale} in our model. We note that our best estimates of J_{scale} are about a factor of 4-5 higher than the corresponding scaling coefficient estimated by Reed et al. (2017) and Ye et al. (2017) based on their box model analysis. This is because simulated NITs mixing ratios at CVAO in our model (median of ~100 pptv) are about 4 times lower than the p-NO_3 mixing ratios (~300-400 pptv) prescribed by Reed et al. (2017) and Ye et al. (2017) in their box models. As noted in Section 3.1, further work is needed to resolve this model discrepancy.

3.3 Impact of NITs photolysis on global NO_x, OH, and O_3

Figure 7 shows the simulated MBL-average distribution of NO_x, OH, and O_3 from the J_{scale}^0 model run, as well as the relative enhancements (relative to the J_{scale}^0 case) of simulated mixing ratios for the J_{scale}^{25} and J_{scale}^{100} model runs. In the J_{scale}^0 simulation, highest MBL mixing ratios of both NO_x and O_3 occur downwind of mid-latitude Northern Hemisphere continental source regions, and, to a lesser spatial extent, downwind of tropical biomass burning regions for O_3. By contrast, highest OH concentrations over oceans occur between 30°S-30°N, reflecting the latitudinal pattern of primary OH production from O_3 photolysis.

As expected, the additional source of NO_x from NITs photolysis in the J_{scale}^{25} and J_{scale}^{100} model runs leads to enhancements in simulated NO_x, OH, and O_3 concentrations in the MBL. Downwind of continental regions, MBL NO_x mixing ratios increase by 5-50 pptv in the J_{scale}^{25} simulation, and by 10-100 pptv in the J_{scale}^{100} simulation, relative to the J_{scale}^0 simulation (Fig. S2). MBL OH mixing ratios increase by 10^5-10^6 molecule cm^{-3}, and MBL O_3 mixing ratio increase by 1-5 ppbv over these same regions (Fig. S2). The simulated relative impact of NITs photolysis peaks over the tropical and subtropical oceans, with enhancement factors ranging from 5-20 for NO_x, 1.2-1.6 for OH, and 1.1-1.3 for O_3 (Fig. 7). The spatial pattern of these relative enhancements due to NITs photolysis is thus very different from the spatial distribution of NITs itself (see Fig. 2). The importance of the tropics is due to intense solar radiation and high temperatures. These conditions lead to an enhanced source of NO_x from nitrate photolysis, together with a reduced source from organic nitrates which have a short lifetime in the warmer air and so have lower concentrations over the remote oceans. This can be understood by comparing the spatial pattern of the chemical production rate of NO_x from NITs photolysis in the J_{scale}^{25} and J_{scale}^{100} model runs with the spatial pattern of the chemical production rate of NO_x from PAN decomposition in the J_{scale}^0 model run, as shown in Fig. 8. In the MBL at Northern Hemisphere mid-latitudes, the chemical source of NO_x from PAN decomposition in the J_{scale}^0 simulation is generally much larger than the source from NITs photolysis in the J_{scale}^{25} simulation. This is also true for the upper-limit J_{scale}^{100} simulation, though to a lesser extent. By contrast, the NO_x source from NITs photolysis is significantly larger than the NO_x source from PAN decomposition over most of the tropical MBL. Inclusion of NITs photolysis in the model therefore more significantly impacts NO_x chemical production, and consequently, simulated NO_x mixing ratios, in the tropical MBL.

We further infer that the source of MBL NO$_x$ from long-range transport of PAN does not change significantly when NITs photolysis is included in the model. Above the MBL, maximum increases in PAN concentrations range from 2-5% and 5-10% for the J_{scale}^{25} and J_{scale}^{100} simulations, respectively, relative to the J_{scale}^0 simulation. The impact of the additional NO$_x$ source from NITs photolysis on MBL NO$_x$ mixing ratios is modulated by the reduction in NO$_x$ lifetime due to the increase in model OH when NITs photolysis is included (see Fig. 7). We also note that the inclusion of NITs photolysis improves the simulation of O$_3$ at CVAO (Fig. 9), offsetting to some extent the simulated effect of halogen-mediated chemical loss of O$_3$ (Sherwen et al., 2016b) in the MBL.

While the inclusion of NITs photolysis is important in terms of modeled NO$_x$, OH, and O$_3$ in the tropical marine atmosphere, it is important to note that its significance is limited to the boundary layer owing to the short lifetime of coarse-mode SSA, and thus of NITs, against deposition. This is illustrated in Fig. 10, which shows simulated enhancements in NO$_x$, O$_3$, and OH due to NITs photolysis for a vertical cross-section at 20° W. In all cases, the impact of NITs photolysis on NO$_x$, OH, and O$_3$ is significant only for altitudes below 1.5-2 km. Very little coarse-mode SSA gets out of the boundary layer and so the impact of NITs photolysis is limited to essentially the MBL. This limits the global impact of this new process. Although Fig. 9 shows some large changes in MBL concentrations, when averaged over the whole troposphere these changes are relatively small. Relative to the J_{scale}^0 model run, increases in the tropospheric masses of NO$_x$, OH, and O$_3$ in the J_{scale}^{25} (J_{scale}^{100}) model runs are 0.6 % (1.7 %), 1.1% (2.9 %), and 0.5% (1.4 %), respectively.

If photolysis of accumulation-mode SSA nitrate had been included, the impacts on MBL NO$_x$ (in terms of relative changes in concentration) would be more wide-spread, especially over remote Southern Hemisphere oceans where a significant fraction of modeled nitrate is in the accumulation-mode (Fig. S1). The impact in the vertical will likely still be limited, owing to the relatively short lifetime (~1 day) of accumulation-mode SSA against deposition (Jaeglé et al., 2011).

3.4 Impact of accumulation-mode p-NO$_3$ photolysis in continental regions

Although much of the recent research emphasis has been on the photolysis of nitrate in SSA, there is some evidence that this might be a more general phenomenon and that p-NO$_3$ photolysis may also occur in other aerosol types. For example, Ye et al. (2018) found p-NO$_3$ photolysis to be a significant source of HONO in background terrestrial air masses over the southern United States. In order to illustrate the potential large-scale impact of this process, we performed one additional simulation in which we allow for photolysis of both NITs and accumulation-mode nitrate (identified as "NIT" in the model). This accumulation-mode aerosol, composed of sulfate, ammonium, and nitrate, is the dominant form of p-NO$_3$ over continental regions. In this simulation, we set the photolysis rate scaling coefficient (i.e. J_{scale}) to be 25 (chosen for illustrative purposes) for both NIT and NITs, and assume that the HONO:NO$_2$ molar yield is 0.67:0.33 as in the J_{scale}^{25} simulation. We refer to this

simulation by the notation J^{25*}_{scale}. The effect of NIT photolysis is isolated by comparing the J^{25*}_{scale} simulation with the J^{25}_{scale} simulation.

Figure 11 shows simulated annual-average NIT and NO_x mixing ratios in the boundary layer from the J^{25}_{scale} simulation, and
5   the change in these mixing ratios when NIT photolysis is included in the J^{25*}_{scale} simulation. Simulated NIT and NO_x mixing ratios are highest (> 1 ppbv) in the eastern United States, western Europe, eastern China, and northern India. Adding NIT photolysis decreases NIT mixing ratios by around 0.01-0.1 ppbv in these regions. Surprisingly, the expected increase in NO_x from NIT photolysis is seen in the model results only in northern India. In fact, adding NIT photolysis decreases simulated NO_x in the eastern United States, western Europe, and most notably in eastern China. There are also a few model grid boxes,
10   especially in southern India and eastern China, where NIT mixing ratios increase when NIT photolysis is included. These counterintuitive features are due to the fact that p-NO_3 photolysis is also a source of OH, and NIT photolysis increases OH in all continental source regions (Fig. 12). The net impact of NIT photolysis on NO_x in a region is determined by the balance between the relative importance of the increased NO_x source due to NIT photolysis and the decreased NO_x lifetime due to the increase in OH. The balance between these two counteracting effects on NO_x varies from region to region in the model. In all
15   cases though, adding NIT photolysis leads to an increase of 1-2 ppbv in O_3 in most regions, with larger increases (>6 ppbv) seen in northern India and eastern China. From a tropospheric average perspective, the impact of NIT photolysis is significantly larger than the impact of NITs photolysis. Relative to the J^{25}_{scale} model run, increases in the tropospheric masses of NO_x, OH, and O_3 in the J^{25*}_{scale} model run are 2.8 %, 4.6 %, and 2.6 %, respectively.

20   Our results highlight the potential importance of p-NO_3 photolysis in continental high-NO_x source regions. We note, however, that the coarse model resolution used in this study cannot resolve important chemical gradients in continental source regions. If further field studies convincingly demonstrate the occurrence of p-NO_3 photolysis on aerosols other than SSA, finer resolution regional model simulations will be needed to more accurately assess the effect of p-NO_3 photolysis on continental boundary layer oxidant chemistry.

25   **4. Conclusions**

We have presented the first global perspective of the impact of NITs photolysis on MBL oxidation chemistry. Comparisons with measurements at CVAO shows that this mechanism is important in terms of explaining some observed aspects of MBL oxidant chemistry. Specifically, we find that the diurnal variation of both HONO and NO_x at CVAO, as well as the absolute magnitude of HONO mixing ratios, are consistent with a NITs photolysis coefficient that is about 25-100 times larger than the
30   corresponding gas-phase HNO_3 photolysis coefficient. Relative to a base case simulation with no NITs photolysis, simulations with NITs photolysis coefficients of this magnitude result in peak relative enhancements ranging from factors of 5-20 for NO_x,

1.2-1.6 for OH, and 1.1-1.3 for O_3 in the tropical and subtropical marine boundary layer. We have also presented preliminary analysis showing the potential importance of p-NO_3 photolysis for continental boundary layer oxidant chemistry.

We emphasize that our analysis of the impact of NITs photolysis on MBL oxidation chemistry is constrained by measurements only at CVAO. Our focus on CVAO is due to the availability of concurrent measurements of relevant chemical species (NO_x, HNO_3, p-NO_3, and HONO) needed to evaluate the model representation of NO_x cycling in the MBL. Our results therefore point to the need for extending and enhancing the MBL NO_x chemistry measurements at CVAO, and for the need for similar long-term measurements in other marine environments. In particular, accurate measurements of the diurnal variation of HONO at a variety of MBL locations can provide further insight into the impact of NITs photolysis on reactive nitrogen cycling over oceanic regions. From a mechanistic perspective, laboratory and field measurements are needed to better understand the mechanism and rates of ambient p-NO_3 photolysis, including the extent to which nitrate photolysis may occur on other aerosol types over both land and ocean regions. Further model developments are also needed to delineate the fraction of nitrate associated with fine-mode sea-salt aerosol and to better couple the calculation of acid uptake on sea-salt aerosols with the MBL halogen chemistry mechanism used in the model. High resolution regional model studies are needed to better understand impacts of nitrate photolysis in continental source regions. Future model studies will be needed to assess the implications of p-NO_3 photolysis with regards to interpreting oxygen isotopic composition measurements of nitrate (Alexander et al., 2009; Savarino et al., 2013) and assessing changes in the tropospheric O_3 distribution from pre-industrial to present.

5. Data availability

Request for the specific version of the model code and model output should be addressed to Prasad Kasibhatla (psk9@duke.edu). The statistical measurement summaries used in Figure 1 are available in the papers referenced in the figure caption. Measurements from CVAO (Figures 3-6, 9) are available from the Centre for Environmental Data Analysis (CEDA, http://www.ceda.ac.uk/).

Acknowledgements

TS, MJE, LJC, CR, JDL, KAR acknowledge the financial support of the National Centre for Atmospheric Science (NCAS) for maintaining CVAO and the Natural Environmental Research Council (NERC) though grants NE/L01291X/1, NE/E011330/1, and NE/D006554/1. The 2015 HONO measurements at CVAO were support by the NERC project SNAABL, NE/M013545/1. BA acknowledges funding from the National Science Foundation through award AGS-1446904. Financial support for the University of Virginia was provided by the National Science Foundation through awards AGS-0328342 and AGS-0646854. Financial support for the University of New Hampshire was provided by the National Science Foundation through awards AGS-0328389 and AGS-0646864.

References

Alexander, B., Savarino, J., Lee, C. C. W., Park, R. J., Jacob, D. J., Li, Q., Thiemens, M. H., and Yantosca, R. M.: Sulfate formation in sea-salt aerosols: Constraints from oxygen isotopes, J. Geophys. Res., 110, D1030, doi:10.1029/2004JD005659, 2005.

5 Alexander, B., Hastings, M. G., Allman, D. J., Dachs, J., Thornton, J. A., and Kunasek, S. A.: Quantifying atmospheric nitrate formation pathways based on a global model of the oxygen isotopic composition ($\Delta^{17}O$) of atmospheric nitrate, Atmos. Chem. Phys., 9, 5043–5056, doi:10.5194/acp-9-5043-2009, 2009.

Beirle, S., Platt, U., von Glasow, R., Wenig, M., and Wagner T.: Estimate of nitrogen oxide emissions from shipping by satellite remote sensing, Geophys. Res. Lett., 31, L18102, doi:10.1029/2004GL020312, 2004.

10 Bey, I., Jacob, D. J., Yantosca, R. M., Logan, J. A., Field, B. D., Fiore, A. M., Li, Q., Liu, H. Y., Mickley, L. J., and Schultz, M. G.: Global modeling of tropospheric chemistry with assimilated meteorology: Model description and evaluation, J. Geophys. Res., 106, 23073–23095, doi:10.1029/2001JD000807, 2001.

Carpenter, L. J., Fleming, Z. L., Read, K. A., Lee, J. D., Moller, S. J., Hopkins, J. R., Purvis, R. M., Lewis, A. C., Müller, K., Heinold, B., Herrmann, H. Fomba, K. W., van Pinxteren, D., Müller, C., Tegen, I., Wiedensohler, A., Müller, T.,
15 Niedermeier, N., Achterberg, E. P., Patey, M. D., Kozlova, E. A., Heimann, M., Heard, D. E., Plane, J. M. C., Mahajan, A., Oetjen, H., Ingham, T., Stone, D., Whalley, L. K., Evans, M. J., Pilling, M. J., Leigh, R. J., Monks, P. S., Karunaharan, A., Vaughan, S., Arnold, S. R., Tschritter, J., Pöhler, D., Frieß, U., Holla, R., Mendes, L. M., Lopez, H., Faria, B., Manning, A. J., and Wallace, D. W. R.: Seasonal characteristics of tropical marine boundary layer air measured at the Cape Verde Atmospheric Observatory, J Atmos. Chem., 67, 87–140, doi:10.1007/s10874-011-9206-1, 2010.

20 Chen, H., Navea, J. G., Young, M. A., and Grassian, V. H.: Heterogeneous photochemistry of trace atmospheric gases with components of mineral dust aerosol, J. Phys. Chem. A, 115, 490–499, doi:10.1021/jp110164j, 2011.

Davis, D. D., Grodzinsky, G., Kasibhatla, P., Crawford, J., Chen, G., Liu, S., Bandy, A., Thornton, D., Guan, H., and Sandholm, S.: Impact of ship emissions on marine boundary layer NO_x and SO_2 distributions over the Pacific Basin, Geophys. Res. Lett., 28, 235–238, doi:10.1029/2000GL012013, 2001.

25 Drummond, J. W., Volz, A., and Ehhalt, D. H.: An optimized chemiluminescence detector for tropospheric NO measurements, J. Atmos. Chem., 2(3), 287–306, doi:10.1007/BF00051078, 1985.

Fairlie, T. D., Jacob, D. J., and Park, R. J.: The impact of transpacific transport of mineral dust in the United States, Atmos. Environ., 41, 1251–1266, doi:10.1016/j.atmosenv.2006.09.048, 2007.

Feng, Y. and J. E. Penner, J. E.: Global modeling of nitrate and ammonium: Interaction of aerosols and tropospheric chemistry,
30 J. Geophys. Res., 112, D01304, doi:10.1029/2005JD006404, 2007.

Fomba, K. W., Müller, K., van Pinxteren, D., Poulain, L., van Pinxteren, M., and Herrmann, H.: Long-term chemical characterization of tropical and marine aerosols at the Cape Verde Atmospheric Observatory (CVAO) from 2007 to 2011, Atmos. Chem. Phys., 14, 8883–8904, doi:10.5194/acp-14-8883-2014, 2014.

Ford, B. and Heald, C.L.: An A-Train and model perspective on the vertical distribution of aerosols and CO in the Northern Hemisphere, J. Geophys. Res., 117, D06211, doi:10.1029/2011JD016977, 2012.

Fountoukis, C. and Nenes, A.: ISORROPIA II: a computationally efficient thermodynamic equilibrium model for K^+–Ca^{2+}–Mg^{2+}–NH_4^+–Na^+–SO_4^{2-}–NO_3^-–Cl^-–H_2O aerosols, Atmos. Chem. Phys., 7, 4639–4659, doi:10.5194/acp-7-4639-2007, 2007.

Fuchs, N. A. and A. G. Sutugin: High dispersed aerosols, in: Topics in Current Aerosol Research (Part 2), edited by: Hidy, G. M. and Brock, J. R., Pergamon, New York, 1971.

Gong, S. L.: A parameterization of sea-salt aerosol source function for sub- and super-micron particles, Global Biogeochem. Cy., 17(4), 1097, doi:10.1029/2003GB002079, 2003.

Guimbaud, C., Arens, F., Gutzwiller, L., Gäggeler, H. W., and Ammann, M.: Uptake of HNO_3 to deliquescent sea-salt particles: a study using the short-lived radioactive isotope tracer ^{13}N, Atmos. Chem. Phys., 2, 249–257, doi:10.5194/acp-2-249-2002, 2002.

Gurciullo, C., Lerner, B., Sievering, H., and Pandis, S. N.: Heterogeneous sulfate production in the remote marine environment: Cloud processing and sea-salt particle contributions, J. Geophys. Res., 104(D17), 21719–21731, doi:10.1029/1999JD900082, 1999.

Handley, S. R., Clifford, D., and Donaldson, D. J.: Photochemical loss of nitric acid on organic films: a possible recycling mechanism for NO_x, Environ. Sci. Technol., 41, 3898–3903, doi:10.1021/es062044z, 2007.

Heland, J., Kleffmann, J., Kurtenbach, R., and Wiesen, P.: A new instrument to measure gaseous nitrous acid (HONO) in the atmosphere, Environ. Sci. Technol., 35, 3207–3212, doi:10.1021/es000303t, 2001.

Hunter, J.: Matplotlib: A 2D graphics environment, Computing In Science & Engineering, 9(3), 90–95, 2007.

Jacob, D. J.: Heterogenous chemistry and tropospheric ozone, Atmos. Environ., 34, 2131–2159, doi:10.1016/S1352-2310(99)00462-8, 2000.

Jaeglé, L., Quinn, P. K., Bates, T. S., Alexander, B., and Lin, J.-T.: Global distribution of sea salt aerosols: new constraints from in situ and remote sensing observations, Atmos. Chem. Phys., 11, 3137–3157, doi:10.5194/acp-11-3137-2011, 2011.

Kasibhatla, P., Levy II, H., Moxim, W. J., Pandis, S. N., Corbett, J. J., Peterson, M. C., Honrath, R. E., Frost, G. J., Knapp, K., Parrish, D. D., and Ryerson, T. B.: Do emissions from ships have a significant impact on concentrations of nitrogen oxides in the marine boundary layer?, Geophys. Res. Lett., 27, 2229–2232, doi:10.1029/2000GL011387, 2000.

Keene, W. C., Talbot, R. W., Andreae, M. O., Beecher, K., Berresheim, H., Castro, M., Farmer, J. C., Galloway, J. N., Hoffman, M. R., Li, S.–M., Maben, J. R., Munger, J. W., Norton, R. P., Pszenny, A. A. P., Puxbaum, H., Westberg, H., and Winiwarter, W.: An intercomparison of measurement systems for vapor- and particulate-phase concentrations of formic and acetic acids, J. Geophys. Res., 94, 6457–6471, doi:10.1029/JD094iD05p06457, 1989.

Keene, W. C., Pszenny, A. A. P., Jacob, D. J., Duce, R. A., Galloway, J. N., Schultz-Tokos, J. J., Sievering, H., and Boatman, J. F.: The geochemical cycling of reactive chlorine through the marine troposphere, Global Biogeochem. Cycles, 4, 407–430, doi:10.1029/GB004i004p00407, 1990.

Keene, W. C., Lobert, J. M., Crutzen, P. J., Maben, J. R., Scharffe, D. H., Landmann, T., Hély, C., and Brain, C.: Emissions of major gaseous and particulate species during experimental burns of southern African biomass, J. Geophys. Res., 111, D04301, doi:10.1029/2005JD006319, 2006.

Keene, W. C., Stutz, J., Pszenny, A. A. P., Maben, J. R., Fischer, E. V., Smith, A. M., von Glasow, R., Pechtl, S., Sive, B. C., and Varner, R. K.: Inorganic chlorine and bromine in coastal New England air during summer, J. Geophys. Res., 112, D10S12, doi:10.1029/2006JD007689, 2007.

Keene, W. C., Long, M. S., Pszenny, A. A. P., Sander, R., Maben, J. R., Wall, A. J., O'Halloran, T. L., Kerkweg, A., Fischer, E. V., and Schrems, O.: Latitudinal variation in the multiphase chemical processing of inorganic halogens and related species over the eastern North and South Atlantic Oceans, Atmos. Chem. Phys., 9, 7361–7385, doi:10.5194/acp-9-7361-2009, 2009.

Kleffmann, J., Lörzer, J. C., Wiesen, P., Kern, C., Trick, S., Volkamer, R., Rodenas, M., and Wirtz, K.: Intercomparison of the DOAS and LOPAP techniques for the detection of nitrous acid (HONO), Atmos. Environ. 40, 3640–3652, doi: 10.1016/j.atmosenv.2006.03.027, 2006.

Kleffmann, J. and Wiesen, P.: Technical Note: Quantification of interferences of wet chemical HONO LOPAP measurements under simulated polar conditions, Atmos. Chem. Phys., 8, 6813–6822, doi:10.5194/acp-8-6813-2008, 2008.

Kraus, A. and Hofzumahaus, A.: Field measurements of atmospheric photolysis frequencies of O_3, NO_2, HCHO, CH_3CHO, H_2O_2, and HONO by UV spectroradiometry, J. Atmos. Chem., 31, 161–180, doi:10.1023/A:1005888220949, 1998.

Laufs, S. and Kleffmann: Investigations on HONO formation from photolysis of adsorbed HNO_3 on quartz glass surfaces, Phys. Chem. Chem. Phys., 18, 9616, doi:10.1039/c6cp00436a, 2016.

Lawler, M. J., Finley, B. D., Keene, W. C., Pszenny, A. A. P., Read, K. A., von Glasow, R., and Saltzman, E. S.: Pollution-enhanced reactive chlorine chemistry in the eastern tropical Atlantic boundary layer, Geophys. Res. Lett., 36, L08810, doi:10.1029/2008GL036666, 2009.

Lawrence, M. G. and Crutzen, P. J.: Influence of NO_x emissions from ships on tropospheric photochemistry and climate, Nature, 402, 6813–6822, doi:10.1038/46013, 1999.

Lee, J. D., Moller, S. J., Read, K. A., Lewis, A. C., Mendes, L. and Carpenter, L. J.: Year-round measurements of nitrogen oxides and ozone in the tropical North Atlantic marine boundary layer, J. Geophys. Res., 114(D21), D21302, doi:10.1029/2009JD011878, 2009.

Lee, J. D., McFiggans, G., Allan, J. D., Baker, A. R., Ball, S. M., Benton, A. K., Carpenter, L. J., Commane, R., Finley, B. D., Evans, M., Fuentes, E., Furneaux, K., Goddard, A., Good, N., Hamilton, J. F., Heard, D. E., Herrmann, H., Hollingsworth, A., Hopkins, J. R., Ingham, T., Irwin, M., Jones, C. E., Jones, R. L., Keene, W. C., Lawler, M. J., Lehmann, S., Lewis, A. C., Long, M. S., Mahajan, A., Methven, J., Moller, S. J., Müller, K., Müller, T., Niedermeier, N., O'Doherty, S., Oetjen, H., Plane, J. M. C., Pszenny, A. A. P., Read, K. A., Saiz-Lopez, A., Saltzman, E. S., Sander, R., von Glasow, R., Whalley, L., Wiedensohler, A., and Young, D.: Reactive Halogens in the Marine Boundary Layer (RHaMBLe): the tropical North Atlantic experiments, Atmos. Chem. Phys., 10, 1031–1055, doi:10.5194/acp-10-1031-2010, 2010.

Leighton, P. A.: Photochemistry of air pollution, Academic Press, University of Michigan., 1961.

Levy II, H., Moxim, W. J., and Kasibhatla, P. S.: A global three-dimensional time-dependent lightning source of tropospheric NO_x, J. Geophys. Res., 101(D17), 22911–22922, doi:10.1029/96JD02341, 1996.

Levy II, H., Moxim, W. J., Klonecki, A. A., and Kasibhatla, P. S.: Simulated tropospheric NO_x: Its evaluation, global distribution and individual source contributions, J. Geophys. Res., 104(D21), 26279–26306, doi:10.1029/1999JD900442, 1999.

Lewis, E. R. and Schwartz, S. E.: Comment on "size distribution of sea-salt emissions as a function of relative humidity", Atmos. Environ., 40, 588–590, doi: 10.1016/j.atmosenv.2005.08.043, 2006.

Long, M. S., Keene, W. C., Easter, R., Sander, R., Liu, X., Kerkweg, A., and Erickson, D. J.: Sensitivity of tropospheric chemical composition to halogen-radical chemistry using a fully coupled size-resolved multiphase chemistry/global climate system: Halogen distributions, aerosol composition, and sensitivity of climate-relevant gases, Atmos. Chem. Phys., 14, 3397–3425, doi.org/10.5194/acp-14-3397-2014, 2014.

Lucchesi, R.: File Specification for GEOS-5 FP. GMAO Office Note No. 4 (Version 1.0), 63 pp., available from https://gmao.gsfc.nasa.gov/pubs/docs/Lucchesi617.pdf, 2013.

McKinney, W.: Data structures for statistical computing in Python, Proceedings of the 9th Python in Science Conference, 51–56, 2010.

Mao, J., Paulot, F., Jacob, D. J., Cohen, R. C., Crounse, J. D., Wennberg, P. O., Keller, C. A., Hudman, R. C., Barkley, M. P., and Horowitz, L. W.: Ozone and organic nitrates over the eastern United States: Sensitivity to isoprene chemistry, J. Geophys. Res. Atmos., 118, 11,256–11,268, doi:10.1002/jgrd.50817, 2013.

Moxim, W. J., Levy II, H., and Kasibhatla, P. S.: Simulated global tropospheric PAN: Its transport and impact on NO_x, J. Geophys. Res., 101(D7), 12621–12638, doi:10.1029/96JD00338, 1996.

Park, R. J., Jacob, D. J., Chin, M., and Martin, R. V.: Sources of carbonaceous aerosols over the United States and implications for natural visibility, J. Geophys. Res., 108(D12), 4355, doi:10.1029/2002JD003190, 2003.

Park, R. J., Jacob, D. J., Field, B. D., Yantosca, R. M. and Chin, M.: Natural and transboundary pollution influences on sulfate-nitrate-ammonium aerosols in the United States: Implications for policy, J. Geophys. Res., 109, D15204, doi:10.1029/2003JD004473, 2004.

Parrella, J. P., Jacob, D. J., Liang, Q., Zhang, Y., Mickley, L. J., Miller, B., Evans, M. J., Yang, X., Pyle, J. A., Theys, N., and Van Roozendael, M.: Tropospheric bromine chemistry: implications for present and pre-industrial ozone and mercury, Atmos. Chem. Phys., 12, 6723–6740, doi:10.5194/acp-12-6723-2012, 2012.

Read, K. R., Mahajan, A. S., Carpenter, L. J., et al.: Extensive halogen-mediated ozone destruction over the tropical Atlantic Ocean, Nature, 453, 1232–1235, doi: 10.1038/nature07035, 2008.

Reed, C., Evans, M. J., Di Carlo, P., Lee, J. D. and Carpenter, L. J.: Interferences in photolytic NO_2 measurements: explanation for an apparent missing oxidant?, Atmos. Chem. Phys., 16(7), 4707–4724, doi:10.5194/acp-16-4707-2016, 2016.

Reed, C., Evans, M. J., Crilley, L. R., Bloss, W. J., Sherwen, T., Read, K. A., Lee, J. D., and Carpenter, L. J.: Evidence for renoxification in the tropical marine boundary layer, Atmos. Chem. Phys., 17, 4081–4092, doi:10.5194/acp-17-4081-2017, 2017.

Sander, R., Pszenny, A. A. P., Keene, W. C., Crete, E., Deegan, B., Long, M. S., Maben, J. R., and Young, A. H.: Gas phase acid, ammonia and aerosol ionic and trace element concentrations at Cape Verde during the Reactive Halogens in the Marine Boundary Layer (RHaMBLe) 2007 intensive sampling period, Earth Syst. Sci. Data, 5, 385–392, doi:10.5194/essd-5-385-2013, 2013.

Savarino, J., Morin, S., Erbland, J., Grannec, F., Patey, M. D., Vicars, W., Alexander, B., and Achterberg, E. P.: Isotopic composition of atmospheric nitrate in a tropical marine boundary layer, P. Natl. Acad. Sci. USA, 110, 17668-17673, doi: 10.1073/pnas.1216639110, 2013.

Schmidt, J. A., Jacob, D. J., Horowitz, et al.: Modeling the observed tropospheric BrO background: Importance of multiphase chemistry and implications for ozone, OH, and mercury, J. Geophys. Res. Atmos., 121, 11819–11835, doi:10.1002/2015JD024229, 2016.

Sherwen, T., Evans, M. J., Carpenter, L. J., Andrews, S. J., Lidster, R. T., Dix, B., Koenig, T. K., Sinreich, R., Ortega, I., Volkamer, R., Saiz-Lopez, A., Prados-Roman, C., Mahajan, A. S., and Ordóñez, C.: Iodine's impact on tropospheric oxidants: a global model study in GEOS-Chem, Atmos. Chem. Phys., 16, 1161–1186, doi:10.5194/acp-16-1161-2016, 2016a.

Sherwen, T., Schmidt, J. A., Evans, M. J., Carpenter, L. J., Großmann, K., Eastham, S. D., Jacob, D. J., Dix, B., Koenig, T. K., Sinreich, R., Ortega, I., Volkamer, R., Saiz-Lopez, A., Prados-Roman, C., Mahajan, A. S., and Ordóñez, C.: Global impacts of tropospheric halogens (Cl, Br, I) on oxidants and composition in GEOS-Chem, Atmos. Chem. Phys., 16, 12239–12271, doi:10.5194/acp-16-12239-2016, 2016b.

Sherwen, T., Evans, M. J., Sommariva, R., Hollis, L. D. J., Ball, S. M., Monks, P. S., Reed, C., Carpenter, L. J., Lee, J. D., Forster, G., Bandy, B., Reeves, C. E., Bloss, W. J.: Effects of halogens on European air-quality, Faraday Discuss., 200, 75–100, doi: 10.1039/C7FD00026J, 2017.

VandenBoer, T. C., Brown, S. S., Murphy, J. G., et al.: Understanding the role of the ground surface in HONO vertical structure: High resolution vertical profiles during NACHTT-11, J. Geophys. Res. Atmos., 118, 10155–10171, doi:10.1002/jgrd.50721, 2013.

van der Walt, S., Colbert, S. C., and Varoquaux, G.: The NumPy array: A structure for efficient numerical computation, Computing in Science & Engineering, 13, 22–30, doi:10.1109/MCSE.2011.37, 2011.

von Glasow, R., von Kuhlmann, R., Lawrence, M. G., Platt, U., and Crutzen, P. J.: Impact of reactive bromine chemistry in the troposphere, Atmos. Chem. Phys., 4, 2481–2497, doi:10.5194/acp-4-2481-2004, 2004.

Waskom, M., Botvinnik, O., O'Kane, D., Hobson, P., Lukauskas, S., Gemperline, D. C., Augspurger, T., Halchenko, Y., Cole, J. B., Warmenhoven, J., de Ruiter, J., Pye, C., Hoyer, S., Vanderplas, J., Villalba, S., Kunter, G., Quintero, E., Bachant, P.,

Martin, M., Meyer, K., Miles, A., Ram, Y., Yarkoni, T., Williams, M. L., Evans, C., Fitzgerald, C., Brian, Fonnesbeck, C., Lee, A., and Qalieh, A.: mwaskom/seaborn: v0.8.1 (September 2017), doi:10.5281/zenodo.883859, 2017.

Willeke, K.: Performance of the slotted impactor, Amer. Indus. Hygiene Assoc. Journal, 36, 683–691, doi: 10.1080/0002889758507315, 1975.

5   Ye, C., Zhou, X., Pu, D., et al.: Rapid cycling of reactive nitrogen in the marine boundary layer, Nature, 532, 489–491, doi:10.1038/nature17195, 2016.

Ye, C., Heard, D. E., and Whalley, L. K.: Evaluation of novel routes for NO_x formation in remote regions, Environ. Sci. Technol., 51, 7442–7449, doi:10.1021/acs.est.6b06441, 2017.

Ye, C., Zhou, X., Pu, D., Stutz, J., Festa, J., Spolaor, M., Tsai, C., Cantrell, C., Mauldin III, R. L., Weinheimer, A., Hornbrook,

10   R. S., Apel, E. C., Guenther, A., Kaser, L., Yuan, B., Karl, T., Haggerty, J., Hall, S., Ullmann, K., Smith, J., and Ortega, J.: Tropospheric HONO Distribution and Chemistry in the Southeast U.S., Atmos. Chem. Phys. Discuss., doi:10.5194/acp-2018-105, in review, 2018.

Zafiriou, O. C. and True, M. B.: Nitrate photolysis in seawater by sunlight, Marine Chemistry, 8, 33–42, doi:10.1016/0304-4203(79)90030-6, 1979.

15   Zhou, X., Gao, H., He, Y., Huang, G., Bertman, S. B., Civerolo, K., and J. Schwab: Nitric acid photolysis on surfaces in low-NOx environments: Significant atmospheric implications, Geophys. Res. Lett., 30, 2217, doi:10.1029/2003GL018620, 2003.

Zhou, X., A. J. Davis, D. J. Kieber, W. C. Keene, J. R. Maben, H. Maring, E. E. Dahl, M. A. Izaguirre, R. Sander, and L. Smoydzyn: Photochemical production of hydroxyl radical and hydroperoxides in water extracts of nascent marine aerosols

20   produced by bursting bubbles from Sargasso seawater, Geophys. Res. Lett., 35, L20803, doi:10.1029/2008GL035418, 2008.
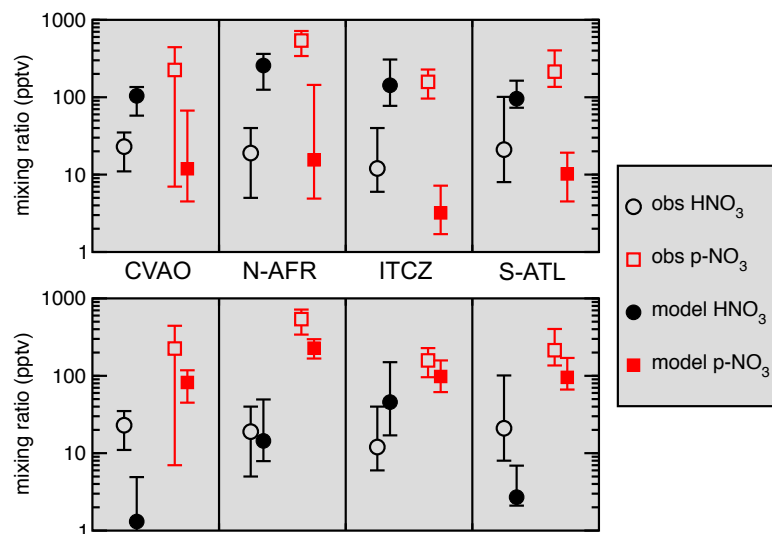
5   Figure 1: Comparison of modeled gas-phase HNO_3 and accumulation- plus coarse-mode particulate nitrate (p-NO_3) from the standard (top panel) and updated (bottom panel) models with measurements. CVAO HNO_3 measurements are for open ocean air masses from the spring 2007 RHaMBLe campaign (Lawler et al., 2009), while p-NO_3 measurements are from the summer marine aerosol subset of samples from 2007-2011 (Fomba et al., 2014). N-AFR, ITCZ, and S-ATL HNO_3 and p-NO_3 ship-board measurements are for the North Africa, ITCZ, and South Atlantic transport regimes in the eastern Atlantic during November 2003 (Keene et al., 2009). Model results are for May (CVAO
10   HNO_3), June-August (CVAO p-NO_3), and November (N-AFR, ITCZ, and S-ATL HNO_3 and p-NO_3) from the 2014-2015 simulations. Symbols and lines indicate means and ranges and/or 2 standard deviations for measurements, and medians and 5th and 95th percentiles of daily means for models.
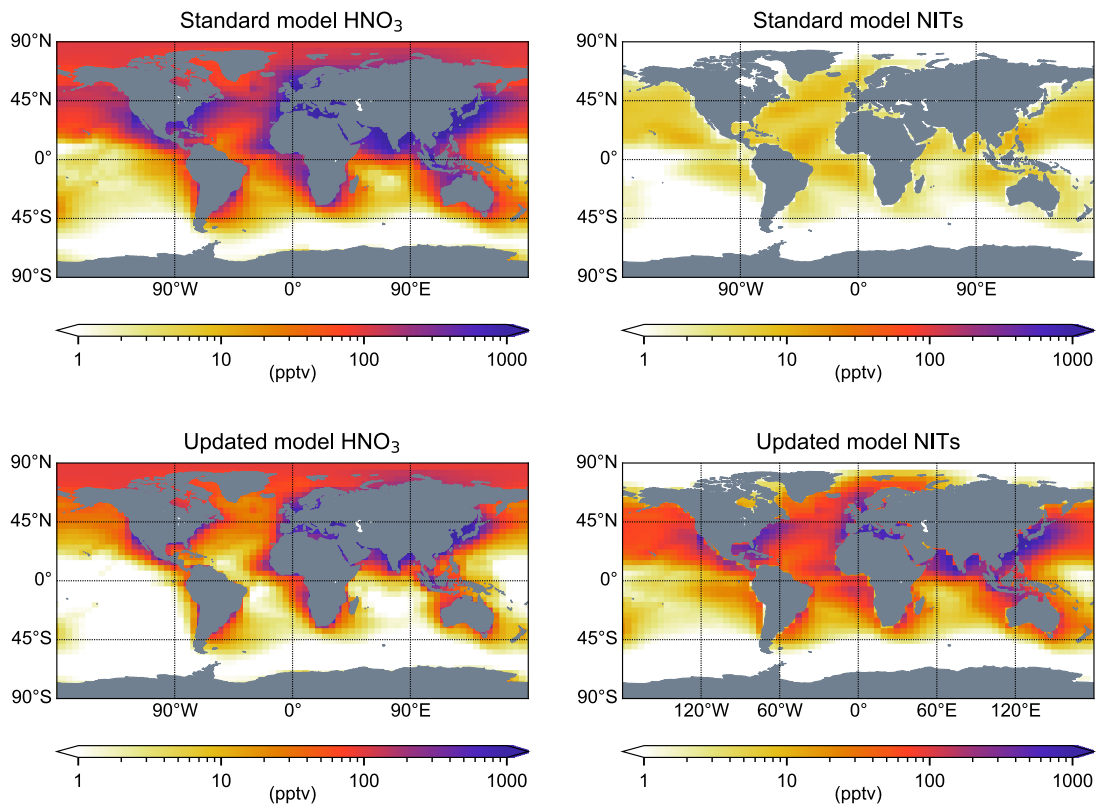
Figure 2: Simulated 2014-2015 MBL-average (average over bottom 1 km) HNO_3 and NITs (p-NO_3 associated with coarse-mode SSA) for the standard and updated models.
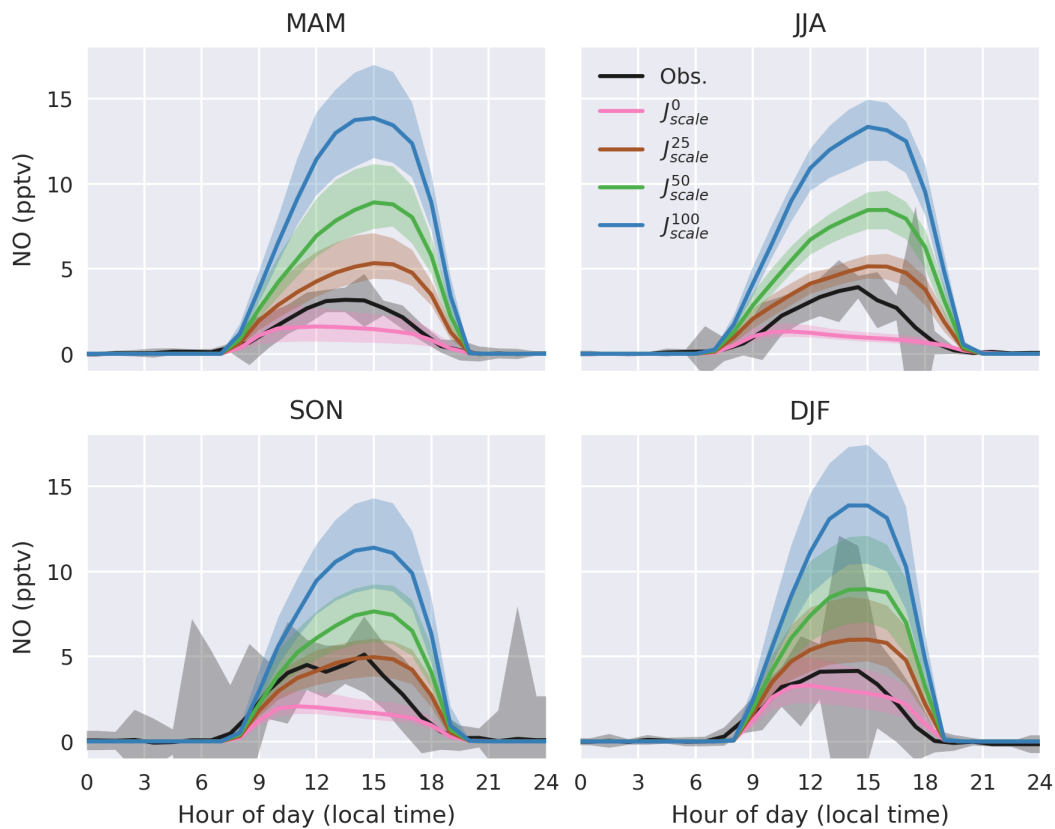
Figure 3: Observed and modeled diurnal cycles of NO at CVAO during different seasons (MAM: March, April, May; JJA: June, July, August; SON: September, October, November; DJF: December, January, February) in 2014-2015. Solid lines represent median values, and shaded regions show 1st and 3rd quartiles of model values and standard error of observations. Model simulations assume a HONO:NO$_2$ molar yield of 0.67:0.33 from NITs photolysis.
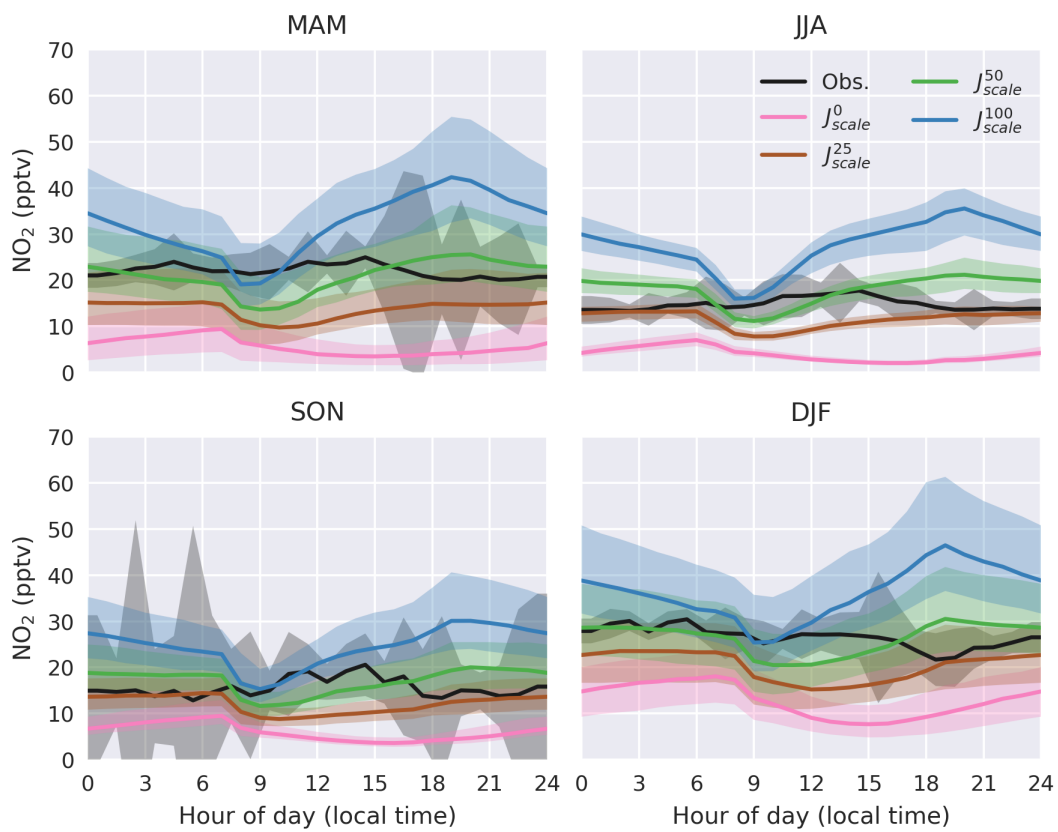
Figure 4: Observed and modeled diurnal cycles of NO_2 at CVAO during different seasons (MAM: March, April, May; JJA: June, July, August; SON: September, October, November; DJF: December, January, February) in 2014-2015. Solid lines represent median values, and shaded regions show 1st and 3rd quartiles of model values and standard error of observations. Model simulations assume a HONO:NO_2 molar yield of 0.67:0.33 from NITs photolysis.
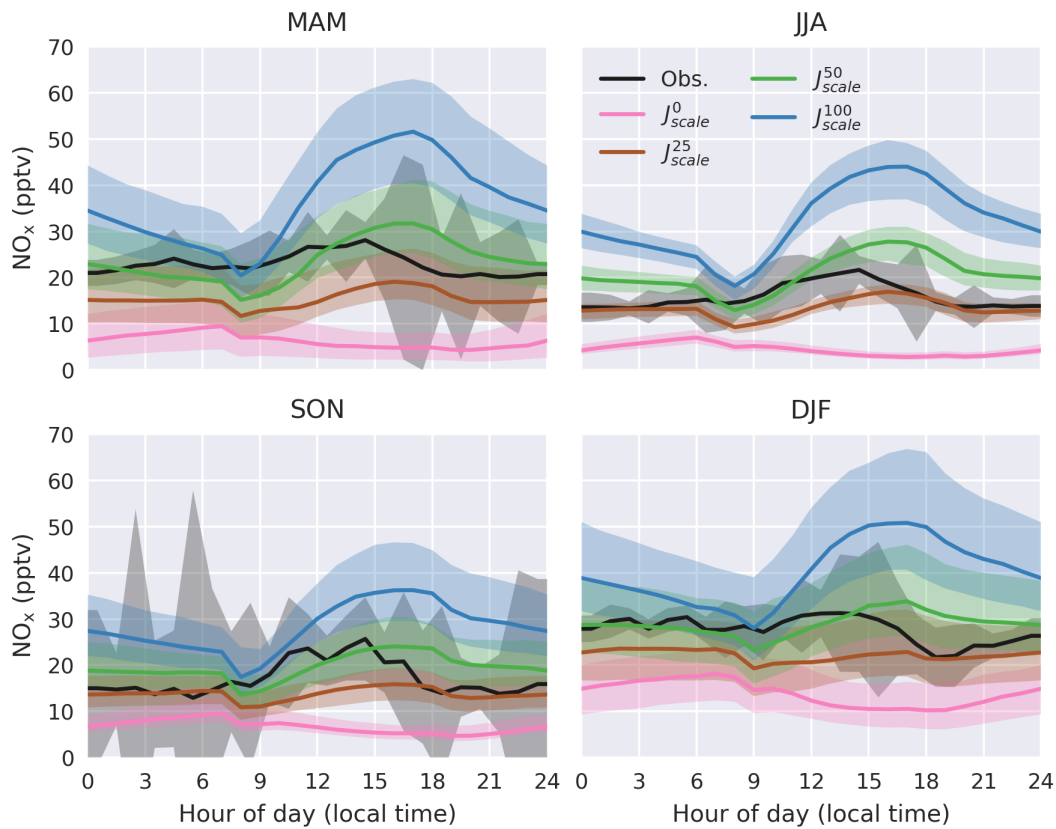
Figure 5: Observed and modeled diurnal cycles of NO_x at CVAO during different seasons (MAM: March, April, May; JJA: June, July, August; SON: September, October, November; DJF: December, January, February) in 2014-2015. Solid lines represent median values, and shaded regions show 1st and 3rd quartiles of model values and standard error of observations. Model simulations assume a $HONO:NO_2$ molar yield of 0.67:0.33 from NITs photolysis.
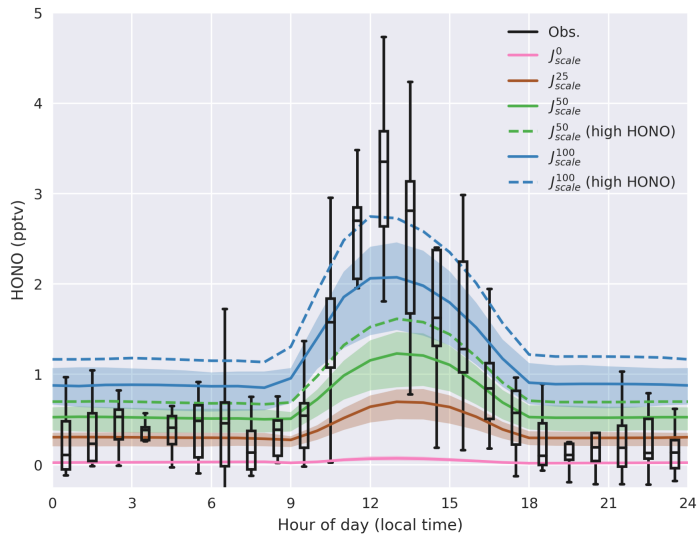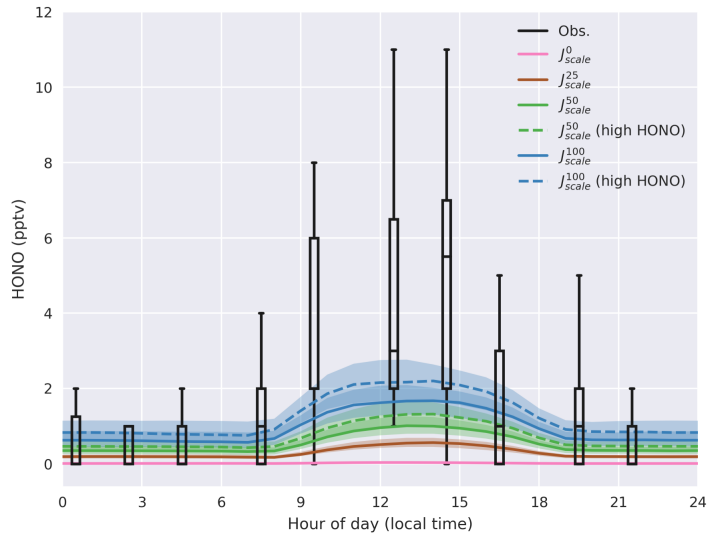
Figure 6: Observed and modeled diurnal cycles of HONO at CVAO. Top panel shown comparison of model results for May from the 2014-2015 simulations with measurements during the spring 2007 RHaMBLe campaign (Sander et al., 2013). Bottom panel shows comparison of model results with measurements (Reed et al., 2017) during November-December 2015. Measurements are shown in box-and-whisker notation, with the box showing the lower and upper quartile values (with a horizontal line at the median) and the whiskers extending to 1.5 times the interquartile range of the data. Solid and dashed lines represent model median values for simulations with a HONO:NO$_2$ molar yield of 0.67:0.33 and 0.93:0.07 (denoted as 'high HONO'), respectively, from NITs photolysis. Shaded regions show 1st and 3rd quartiles of model values.
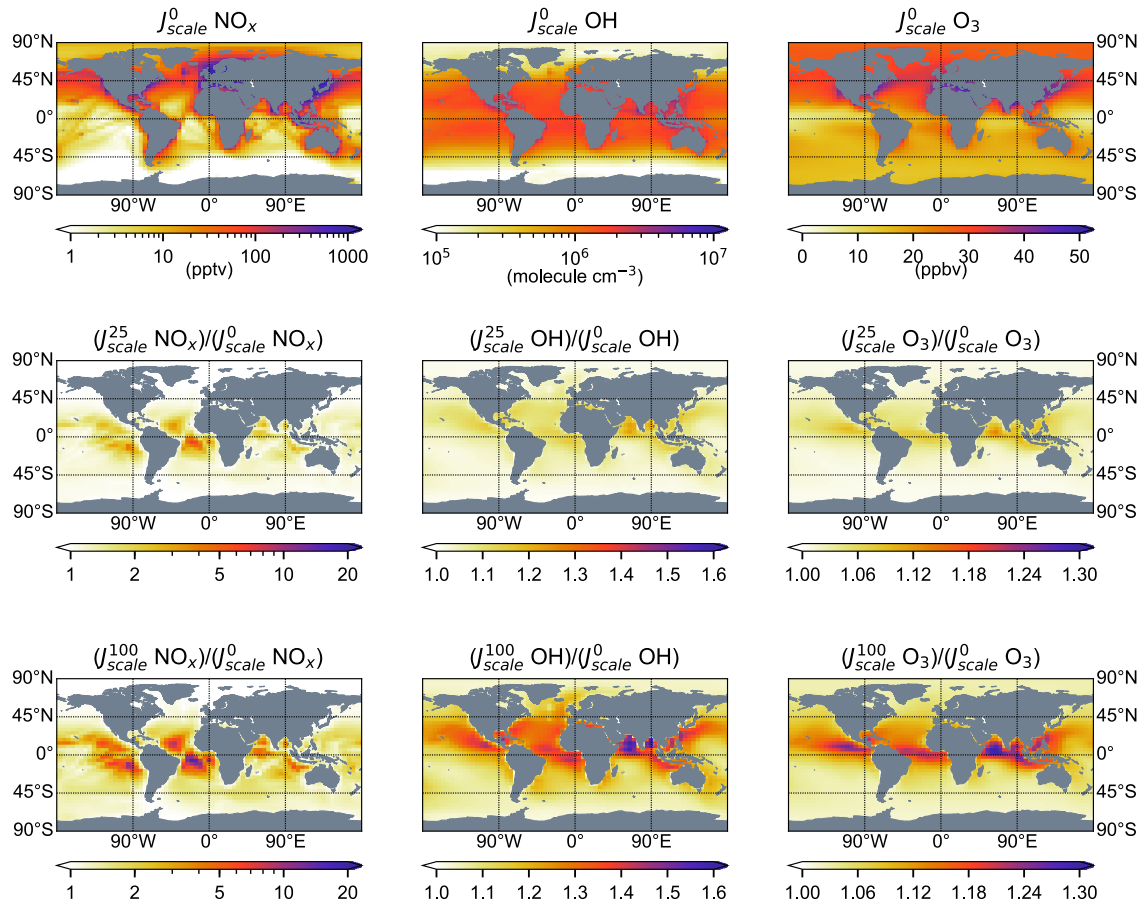
Figure 7: Simulated 2014-2015 MBL-average (average over bottom 1 km) concentrations for the J_{scale}^0 model run (top panels) and ratio of simulated MBL-average concentrations for the J_{scale}^{25} (middle panels) and J_{scale}^{100} (bottom panels) model runs relative to the J_{scale}^0 model run for NO$_x$ (left panels), OH (middle panels) and O$_3$ (right panels).
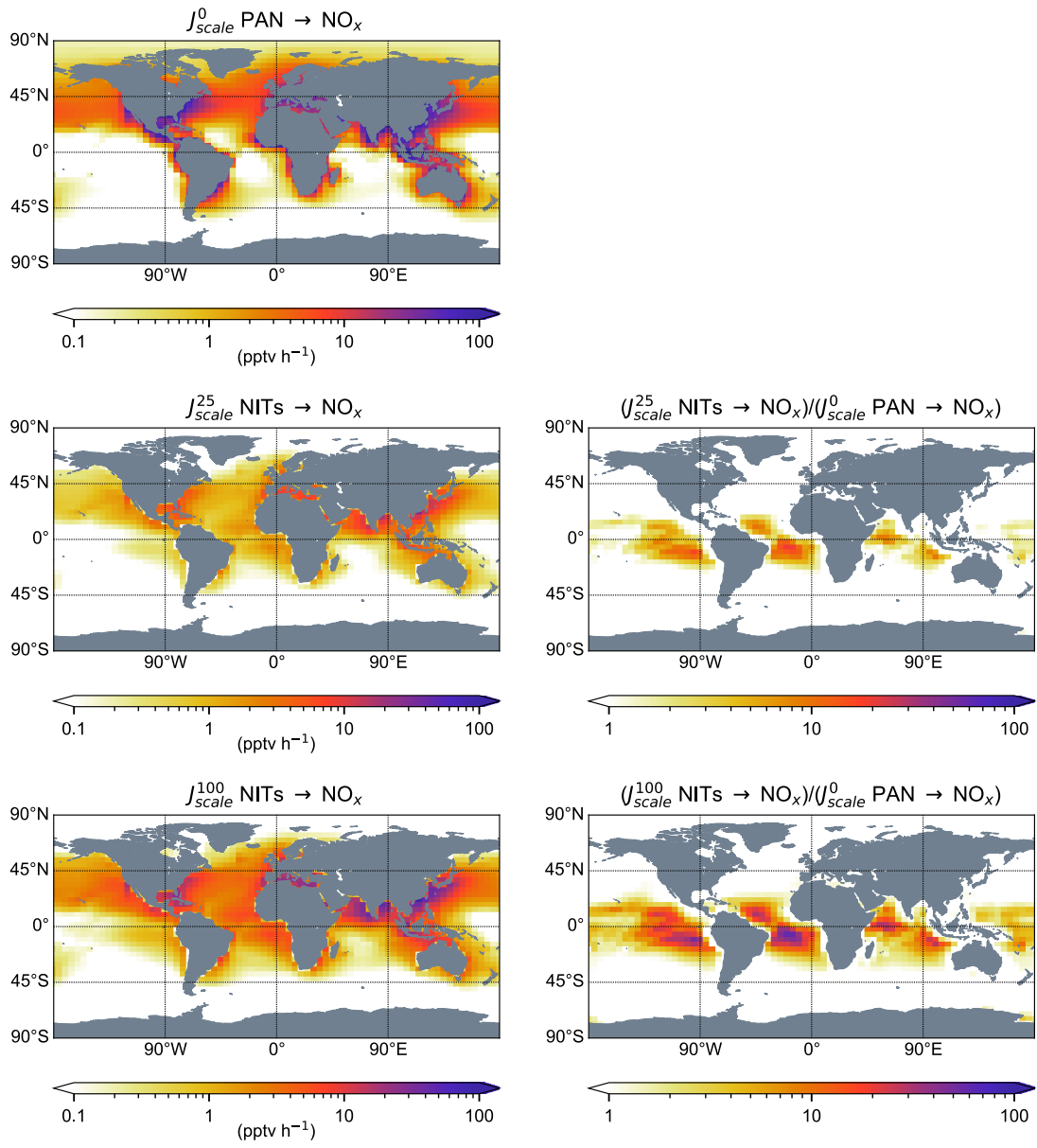
Figure 8: Simulated 2014-2015 MBL-average (average over bottom 1 km) NO_x production rate from PAN decomposition for the J_{scale}^0 model run (top left panel) and from NITs photolysis for the J_{scale}^{25} (middle left panel) and J_{scale}^{100} (bottom left panel) model runs. The ratio of the NO_x production rate from NITs photolysis for the J_{scale}^{25} and J_{scale}^{100} model runs relative to the NO_x production rate from PAN decomposition for the J_{scale}^0 model run is shown in the middle right and bottom right panels, respectively.
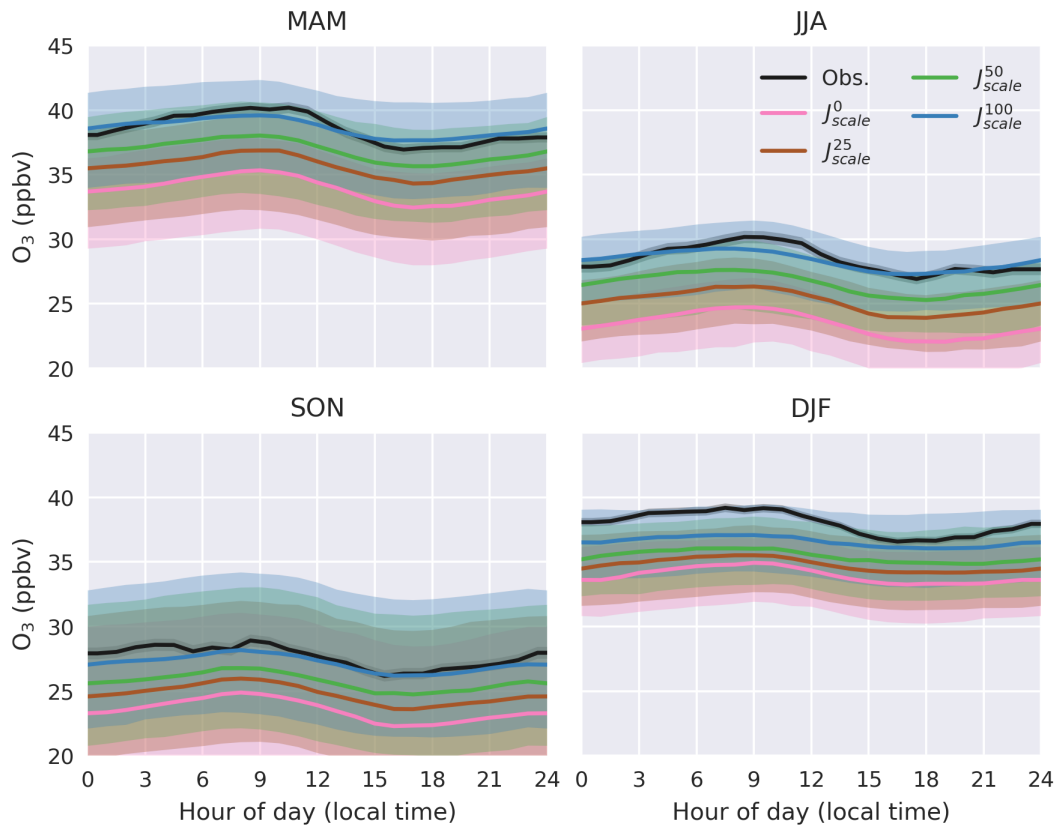
Figure 9: Observed and modeled seasonal cycle of O$_3$ at CVAO during 2014-2015. Solid lines represent median values, and shaded regions show 1st and 3rd quartiles of model values and standard error of observations.
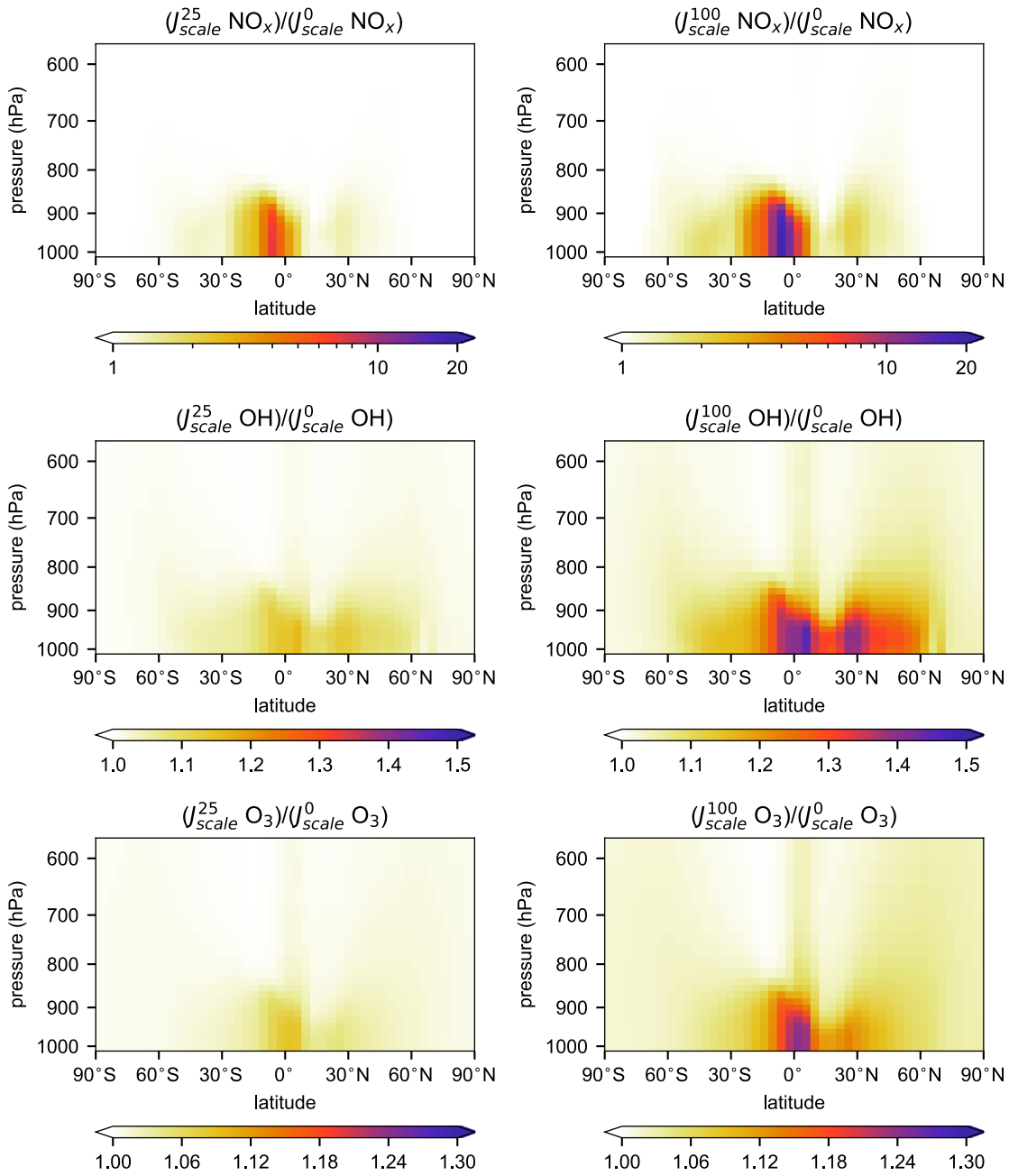
Figure 10: Latitude-altitude plot of average 2014-2015 NO_x (top panels), OH (middle panels), and O_3 (bottom panels) for the J^{25}_{scale} and J^{100}_{scale} model runs (left and right panels, respectively) relative to corresponding fields for the J^0_{scale} model run at 20° W longitude.
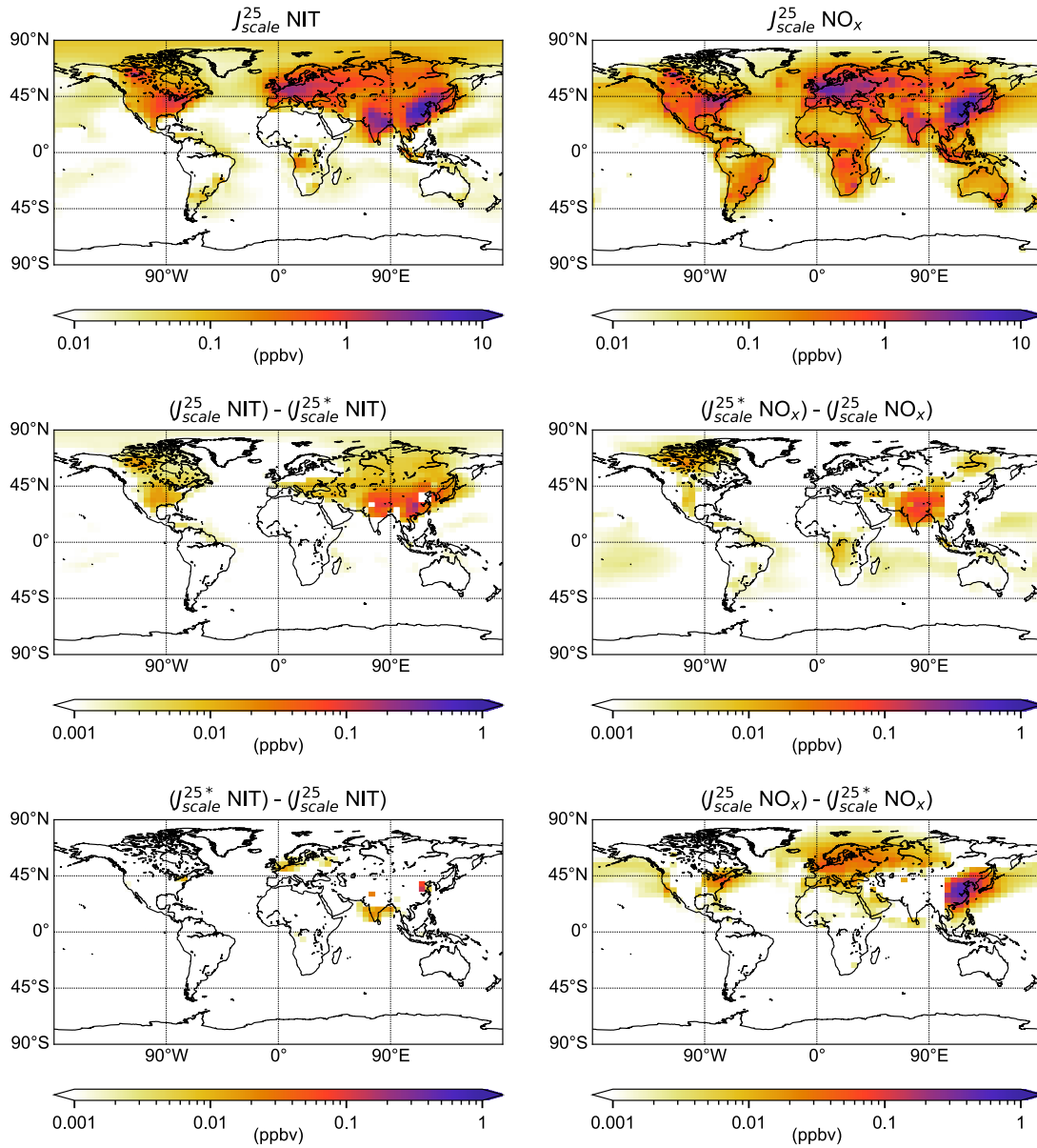
Figure 11: Simulated 2014-2015 boundary layer-average (average over bottom 1 km) accumulation-mode nitrate (NIT) and NO_x mixing ratios for the J_{scale}^{25} model (that includes photolysis of only coarse-mode sea-salt nitrate) and the J_{scale}^{25*} model (that includes photolysis of both coarse-mode sea-salt and accumulation-mode NIT) runs. NIT and NO_x for the J_{scale}^{25} model are shown in the top left and top right panels, respectively. Middle panels show regions where NIT (NO_x) mixing ratios decrease (increase), and bottom panels show regions where NIT (NO_x) mixing ratios increase (decrease), due to accumulation-mode NIT photolysis.
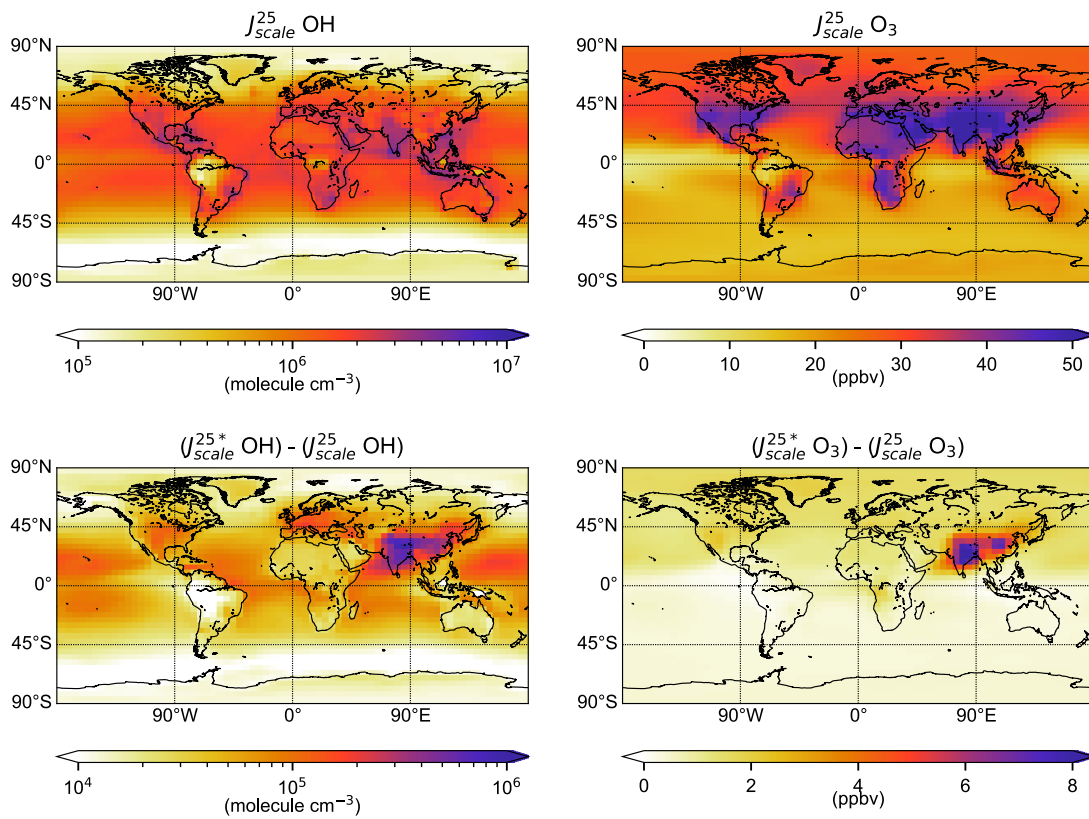
Figure 12: Simulated 2014-2015 boundary layer-average (average over bottom 1 km) OH and O_3 mixing ratios for the J_{scale}^{25} model run (top left and top right panels, respectively), and changes in OH and O_3 mixing ratios ratios (bottom left and bottom right panels, respectively) when NIT photolysis is included.